

# Recent advances in solar data-driven MHD simulations of the formation and evolution of CME flux ropes

Schmieder Brigitte<sup>1,2\*</sup>, Guo Jinhan<sup>1,3†</sup> and Poedts Stefaan<sup>1,4†</sup>

<sup>1\*</sup>CmPA/Dept. of Mathematics, KU Leuven, Celestijnenlaan 200B, Leuven, 3001, Belgium.

<sup>2</sup>LIRA, Observatoire de Paris, 5 place Janssen, Meudon, 92195, Hauts-de-Seine, France.

<sup>3</sup>School of Astronomy and Space Science, Nanjing University, 163 Xianlin Road, Qixia District, Nanjing, 210023, China.

<sup>4</sup>Institute of Physics, University of Maria Curie-Skłodowska, ul. Marii Curie-Skłodowskiej 1, 20-031, Lublin, Poland.

\*Corresponding author(s). E-mail(s): [brigitte.schmieder@obspm.fr](mailto:brigitte.schmieder@obspm.fr);

Contributing authors: [jinhan.guo@kuleuven.be](mailto:jinhan.guo@kuleuven.be);

[stefaan.poedts@kuleuven.be](mailto:stefaan.poedts@kuleuven.be);

†These authors contributed equally to this work.

## Abstract

Filament eruptions and coronal mass ejections are physical phenomena related to magnetic flux ropes carrying electric current. A magnetic flux rope is a key structure for solar eruptions, and when it carries a southward magnetic field component when propagating to the Earth. It is the primary driver of strong geomagnetic storms. As a result, developing a numerical model capable of capturing the entire progression of a flux rope, from its inception to its eruptive phase, is crucial for forecasting adverse space weather. The existence of such flux ropes is revealed by the presence of sigmoids in active regions or hot channels by observations from space and ground instruments. After proposing cartoons in 2D, potential, linear, non-linear-force-free-field (NLFFF) and non-force-free-field (NFFF) magnetic extrapolations, 3D numerical magnetohydrodynamic (MHD) simulation models were developed, first in a static configuration and later dynamic data-driven MHD models using high resolution observed vector magnetograms. This paper reviews a few recent developments in data-driven models,

such as the time-dependent magneto-frictional (TMF) and thermodynamic magnetohydrodynamic (MHD) models. Hereafter, to demonstrate the capacity of these models to reveal the physics of observations, we present the results for three events explored in our group: 1. the eruptive X1.0 flare on 28 October 2021; 2. the filament eruption on 18 August 2022; and 3. the confined X2.2 flare on 6 September 2017. These case studies validate the ability of data-driven models to retrieve observations, including the formation and eruption of flux ropes, 3D magnetic reconnection, CME three-part structures and the failed eruption. Based on these results, we provide some arguments for the formation mechanisms of flux ropes, the physical nature of the CME leading front, and the constraints of failed eruptions.

**Keywords:** solar flares, coronal mass ejections, MHD simulations

## 1 Introduction

Solar eruptions release a large amount of magnetic energy into the solar atmosphere and potentially jeopardise the environment of the interplanetary space. Magnetic energy stored in the solar atmosphere is converted into thermal energy, including emissions across the electromagnetic spectrum, kinetic energy with magnetized plasma ejections called coronal mass ejections (CMEs), and ejections of high-energetic particles (SEPs). The origin of CMEs is identified as eruptions of filaments, sigmoids in active regions, and hot channels (Figure 1) [1–4].

CMEs are commonly modelled by magnetic flux ropes (FRs) [5–7], defined as a coherent group of magnetic field lines winding an axis with more than one turn or by a volume channel full of electric currents formed before or during eruptions (Figure 2). Modelled flux ropes should be consistent with their proxies in observations, such as filaments and hot channels, which are not by themselves a proof of the existence of the FR. Sheared arcades can also have dips and support filaments [8]. Depending on their velocity, CMEs travel through the heliosphere and may produce geomagnetic events after one to 5 days. Therefore, it is essential to forecast them as early as possible [7]. Many attempts have been made to find the progenitors of eruptions close to the sun. Progenitors of CMEs are detected by kinematics properties such as a slow rise or oscillation of a filament [9–14], by thermal signatures with very hot channels [15, 16] and by magnetic flux, e.g., twist increase and magnetic helicity fluctuations [17–21].

Looking at sunspots and observing scarves in the penumbra and umbra could help to detect the “feet” of the flux rope in an eruption stage [30]. Figure 3 (panel a) represents a sketch of the 3D magnetic structures and magnetic field lines found in eruptive active regions modelled with the OHM simulation [27, 28]; the hooks of the ribbons are interpreted as the footprints of the flux rope of the eruption. Another proxy is the observation of hot channels in the corona using the AIA imager on board the Solar Dynamics Observatory (SDO) in hot temperature filters (131 Å and 94 Å) [14]. It was shown that the morphology of the flux rope with a small or large radius observed on the disk is also a precursor for small or large storms [25].

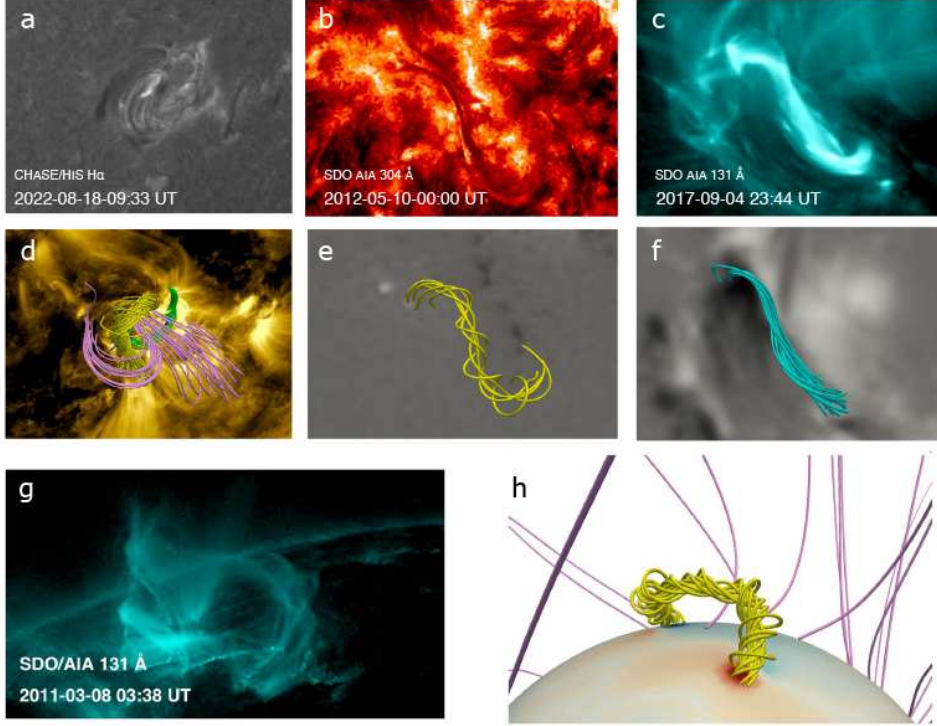


**Fig. 1** Flux rope (FR) observations and corresponding models. Top row: filaments observed on the disk (a) with CHASE, (b) with SDO/AIA in 304 Å, (c) sigmoid observed with SDO/AIA in 131 Å. Middle row: (d) NLFFF extrapolation of magnetic field (adapted from [22]), (e) inserted flux rope (adapted from Guo et al. [23]), (f) FR from MHD simulation similar to the observed sigmoid in panel (c) (adapted from [22]). Bottom row: (g) hot channel observed at the limb [16, 24], (h) MHD simulation of a FR (adapted from Guo et al. [25]).

Solar eruptions have been explained in a first attempt with the 2D standard model (CSHKP) developed between 1964 and 1976 by Carmichael [31], Sturrock and Coppi [32], Hirayama [33], Kopp and Pneuman [34], based on magnetic reconnection in the legs of flux rope or arcades evolving in magnetohydrodynamic (MHD) environment [35]. Magnetic reconnection occurs in non-ideal, highly conducting plasmas where the magnetic field lines are generally frozen to the plasma. The key processes are well present in these standard models, but still, many observable features in 3D are not taken into account. Some magnetic properties cannot be described in the 2D standard model, such as the toroidal and poloidal flux and the twist of the magnetic field in the flux rope. In 2D models, magnetic reconnection occurs in the current sheet induced by a null point. However, the null point becomes unnecessary in the 3D scenario, and magnetic reconnection occurs in the region where magnetic field connectivity changes drastically, namely, the quasi-separatrix layers (QSLs) [36]. The reconnection in QSLs is generally called slipping reconnection, in which the slipping velocity of one field line increases with the local norm  $N$  [37]. QSLs are regions of high distortion of the mapping of magnetic field lines anchored in the photosphere [36, 38]. This distortion

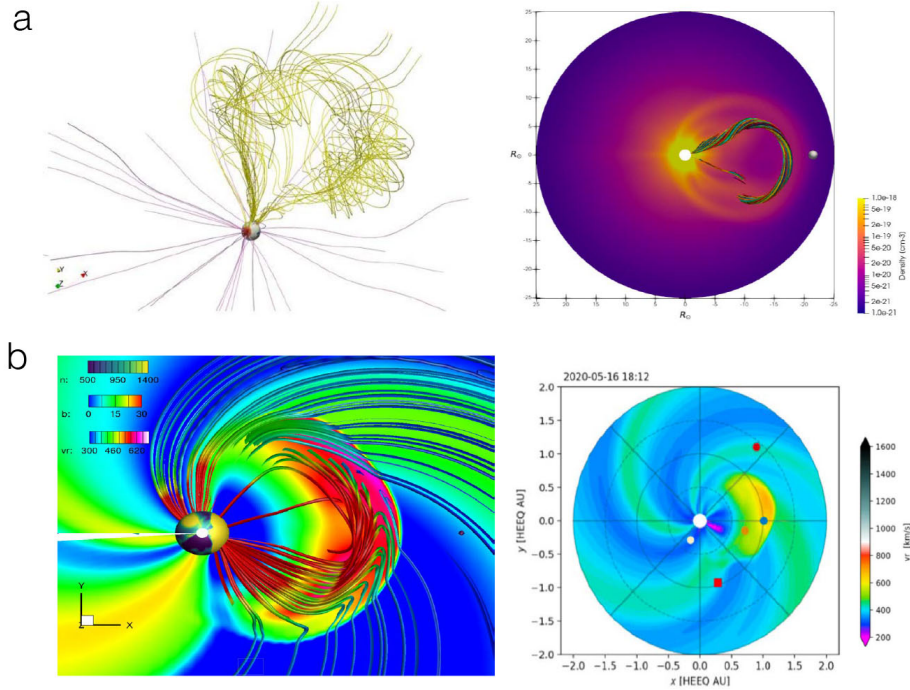


**Fig. 2** Simulations of coronal mass ejections as flux ropes (FR); (a) (left) Flux rope (yellow tubes) in the ambient solar wind (pink tubes) provided by the COCONUT code (adapted from [25]), (right) Density distribution of a FR in the equatorial plane in log scale [26], (b) (left) Magnetic cloud EUHFORIA simulation with FR3D (adapted from [7]). The charts of colours indicate the values of density (d), magnetic field (B), and radial velocity (Vr). (right) Equatorial section of a CME in the heliosphere between the Sun and Earth [7].

is described by derivatives of the field line mapping functions expressed via Jacobian matrices of the MHD equations, and the vertical norm  $N$  is directly related to the squashing factor.

QSLs are layers where current flows easily in response to changes in the plasma. They may contain high electric current-density if neighbouring magnetic field lines can change their different footprint locations drastically. The squashing degree  $Q$  is a parameter that indicates the gradient of connectivity change in the magnetic field volume under consideration [39]. A high squashing factor  $Q$  suggests that the magnetic field is more distorted and that it is more likely to form high electric current densities. Same as the X point in 2D, the 3D reconnection most likely starts in Hyperbolic Flux Tubes (HFT) involving two intersecting QSLs, which comprise two intersecting layers [39, 40]. Each layer arises from a crescent-shaped strip with one pole and tapers toward the other. The crescent-shaped bands connecting two sunspots have the same polarity. The intersections of these domains with the photosphere are characterised by emission enhancements in all wavelength ranges, such as flare ribbons visible in UV and optical ranges and kernels in X-rays during flares and eruptions. The cartoon in

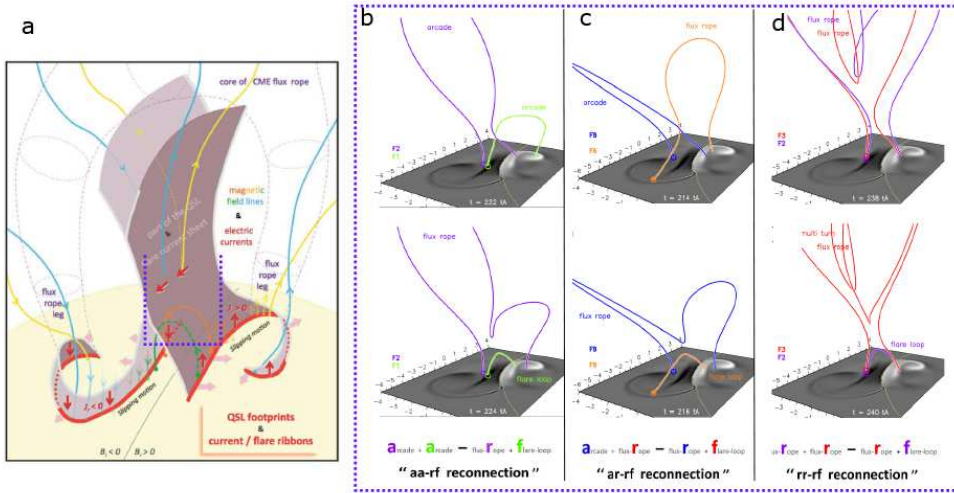


**Fig. 3** (left panel) Sketch of the 3D magnetic structures and magnetic field lines found in eruptive active regions modelled with the OHM simulation [27, 28]; (right panels), the different possibilities of a flux rope to reconnect with arcades, and overlying magnetic field [29].

Figure 3 (top left panel) summarises these magnetic structures observed in 3D and retrieved in the Observationally driven High-order Magnetohydrodynamics (OHM) simulations with the line-tying and zero- $\beta$  approximations [27–29, 41]).

Several 3D MHD simulation models with zero- $\beta$  assumption have been developed nowadays both in bipolar magnetic configuration [27, 41–43] and in multi-polar configurations [44]. In the bipolar model, flux cancellation or shearing motions can build up a flux rope, which is subject to the kink instability or the torus instability leading to the eruption of the FR [43, 45–47]. In the multi-polar configuration, Antiochos et al. [44] and Chen and Shibata [48] proposed the breakout model and emerging flux trigger, respectively.

These models are compelling and recover the main features of flares, incl. the flare ribbons, the post-flare loops, and the site of reconnection [37]. Moreover, in the OHM simulations [29], slipping magnetic reconnection occurs in the HFT structure below the eruptive flux rope. In their simulations, three types of reconnection geometries are recognized: the reconnection ( $aa - rf$ ) refers to reconnection between an Arcade and another Arcade leading to the formation of a flux Rope and a Flare loop, ( $rr - rf$ ) reconnection between a flux Rope and another flux Rope leading to a flux Rope and a Flare loop, ( $ar - rf$ ) reconnection between an Arcade and a flux Rope leading to a flux Rope and a Flare loop. These reconnection geometries can explain many complicated 3D observational phenomena, such as the shift of filament legs [49], saddle-like flare loops [50], footpoint drifting and decrease in toroidal fluxes of CME flux ropes [51]. Additionally, this theoretical model can be applied to ample parameter space, including stars, e.g. to forecast super flares [52].

However, in the zero- $\beta$  models [29, 41, 53–56], or in isothermal MHD models [57, 58], the thermal properties of the plasma are discarded or at least drastically simplified. Therefore, comparing these simulation results with the multi-temperature images of SDO/AIA is difficult.

Recent studies are focused directly on the observations, which leads to data-driven or data-constrained models (see the reviews of Inoue et al. [54], Jiang et al. [59]). In data-driven models, the observational data from the photosphere are taken as inputs for driving the coronal field and the related plasma flows, such as the magnetic fields [57], velocity [46, 60, 61], the combination of the velocity and the magnetic field [47, 62], and the electric field [60, 63–66]. The outcomes of these data-driven or data-constrained models are directly comparable to multi-wavelength observations, demonstrating significant potential in quantitatively elucidating the fundamental physical mechanisms behind the observations [57, 59, 62].

This review is interested in data-constrained and data-driven models exploiting velocity and magnetic field data. Section 2 details the data used to drive the models. Section 3 demonstrates how data-constrained models are achieved in a few case studies. Section 4 is focused on data-driven models and the formation of flux ropes. Section 5 explains the role of the magnetic tension leading to confined flares.

## 2 Data inputs for MHD models

### 2.1 Extrapolation of the magnetic field

Numerous recent studies involving numerical models based directly on observational data have been conducted. The critical question is the distributions of the magnetic field and the electric current in the corona.

Solar magnetographs have been developed to produce photospheric magnetograms from the ground and space with increasingly higher spatial and temporal resolution. The full disk of the magnetograph MDI on board SOHO since 1996 [67] was already a progress, even with only the line-of-sight magnetograms, since 2011 HMI on board SDO [68] allows us to have magnetic field vector-maps every 12 min. The technique of inversion of the Stokes parameters is well developed for HMI data using the Very Fast Inversion of Stokes Vector or UNNOFIT [69, 70], which are Milne–Eddington based algorithms. A minimum energy method [71–73] is used to resolve the 180° ambiguity in the transverse field [71, 72]. The SDO/HMI vector magnetograms must be pre-processed to ensure that the photospheric magnetic field satisfies the NLFFF model assumptions in the local Cartesian coordinate system, as the photosphere is not always force-free. The pre-processing follows the methods developed by Wiegmann et al. [74] and discussed by Valori et al. [75] and Thalmann et al. [76]. All these steps are mathematically not well posed, therefore extrapolations is a difficult task. Measurement of physical parameters can show an ambiguity in the results [76]. Moreover, such pre-processing does not include the projection effects, and central disk eruptions are often considered. Since recently, pre-processing involves correcting the projection effects and removing the Lorentz force and torque [77].

Different methods to improve the magnetic field extrapolation in the corona have been developed using potential field [78], linear-force-free (LFF) [79, 80], non-linear-force-free-field (NLFFF) [81, 82] assumptions. In these studies, the models are restricted to static reconstructions of the nearly force-free coronal magnetic field. With only one magnetogram, obtained just before the eruption, two sets of magnetic field lines are drawn, one corresponding to the magnetic field before the eruption and one corresponding to the magnetic field after reconnection [83]. The large-scale magnetic field configuration does not change significantly during typical solar and confined flares. The observed flare loops involved both before and after the flare can thus be fitted using a single magnetogram [22, 62, 84–88]. Notice that just before the eruption, the field is already well-developed and, by definition, unstable. Hence, using magnetograms immediately preceding the eruption for the coronal magnetic field reconstruction and taking this magnetic field as the initial MHD simulation condition reproduces the erupting field’s fast dynamic phase. The evolution of coronal magnetic fields in the pre-eruption phase and the triggering of the eruption are, however, not revealed in such simulations. It is well accepted that ideal MHD instability and magnetic reconnection are responsible for initiating a CME. Regarding the ideal MHD instability, it incorporates kink instability [89] and torus instability [43], wherein the former are controlled by the twist number of the pre-eruptive flux rope, while the latter is determined by the decaying degree of the overlying background magnetic fields. As for the role of magnetic reconnection in leading to a CME, it is classified into tether-cutting [46, 90], emerging flux [48] and breakout [44] models. Jiang et al. [58] and Duan et al. [6] investigated the role of ideal MHD instability in triggering solar eruptions by computed the twist number and decay index of the pre-eruptive magnetic fields. They found that the threshold of these two metrics can be adopted to distinguish confined and eruptive flares to a great extent, and some exceptions could be due to magnetic reconnection. In particular, Jiang et al. [91] detailed the fundamental role of magnetic reconnection in triggering solar eruptions. Thus, such models do not allow for the identification of the actual trigger and dynamic evolution of solar eruptions.

## 2.2 MHD relaxation Model

In the previously mentioned studies, one magnetogram or a series of magnetograms was used, but the eruption mechanism could only be investigated tentatively because no dynamics were included. Even a time sequence of magnetic fields reconstructed following the coronal evolution does not reflect its intrinsic dynamics because these magnetic fields are treated as independent. By definition, the reconstructed coronal magnetic field immediately before the eruption is unstable.

It is necessary to relax the solar atmosphere, an electrically conductive fluid, to some minimum energy state to study flares [92]. Potential field extrapolations are often used. These are minimum-energy models for the coronal magnetic field of the Sun. NLFFF extrapolations are therefore performed using an MHD relaxation method. Different methods exist we may quote the Zhou et al. [9], Zhu et al. [93], Jiang and Feng [94] and Guo et al. [95, 96] methods. The method described by Zhu et al. [93] and Zhou et al. [9] consists of computing the magnetohydrostatic state of the solar atmosphere. This relaxation is achieved in several case-study events [88].

The CESE–MHD–NLFFF model developed by Jiang et al. [97] is based on an MHD-relaxation method which seeks approximately force-free equilibrium. It solves a set of modified zero- $\beta$  MHD equations with a friction force using an advanced conservation-element/solution-element (CESE) space-time scheme on a nonuniform grid with parallel computing. With this method, 45 flares have been analysed, showing that flux ropes exist in the pre-flare phase, and by computing the twist parameter and the decay index, they show that eruptive and confined flares can be forecast [6]. The Guo method is based on the magneto-friction (MF) relaxation method (see next subsection).

### 2.3 Magneto-frictional method

The magneto-friction method is a simplification of the MHD model, which omits gravity and thermal pressure, and the velocity is assumed to be proportional to the local Lorentz force. As such, the MF method only computes the magneto-induced equation, and the final relaxed state will be converted to a force-free field. The governing equations of the MF relaxation are as follows:

$$\frac{\partial \mathbf{B}}{\partial t} + \nabla \cdot (\mathbf{v}\mathbf{B} - \mathbf{B}\mathbf{v}) = -\nabla \times (\eta\mathbf{j}), \quad (1)$$

$$\mathbf{v} = \frac{1}{\nu} \frac{\mathbf{j} \times \mathbf{B}}{B^2}, \quad (2)$$

where  $\nu$  is the viscous coefficient of the friction and  $\eta$  is the magnetic diffusivity. Hence, this method can extrapolate static coronal NLFFF from the potential field model where the bottom boundary is provided by the observed vector magnetograms in the photosphere, such as Guo et al. [95]. Additionally, to reduce computing expenses and simultaneously obtain the temporary evolution of 3D coronal magnetic fields, many authors have adopted a time-dependent magnetofrictional (TMF) model to perform data-driven models [63, 64, 66, 98–101], where the bottom boundaries are provided by a series of observed magnetograms or their derived electric fields. Compared to other methods for NLFFF extrapolation, such as the optimisation [102, 103] and Grad-Rubin [104–106] methods, the numerical computation of the magneto-frictional relaxation is still based on the numerical schemes of the MHD equations. As a result, it is easier to perform in open-source codes for MHD numerical simulations and coupled with some advanced numerical strategies, i.e., the adaptive mesh refinement (AMR) and stretching grids, constrained-transport (CT) method for keeping magnetic-field divergence freeness introduced in the computation process, and magnetic-field splitting to decrease the numerical diffusion.

Guo et al. [96] made a significant step forward in this domain by the implementation of a magneto-frictional module in the Message Passing Interface Adaptive Mesh Refinement Versatile Advection Code [MPI-AMRVAC<sup>1</sup>, 107, 108]. The magneto-frictional method has also been applied to several case studies. Thus, its applicability has been demonstrated in Cartesian as well as in spherical coordinates and both uniform and

---

<sup>1</sup><http://amrvac.org>



block-adaptive octree grids [23, 95, 109]. Moreover, in NLFFF modelling, local high spatial resolution can be achieved simultaneously with a large field-of-view using parallel and block-adaptive magneto-frictional relaxations [22, 47, 62]. For example, in the paper by Guo et al. [22] concerning the non-radial motion of a filament during its eruption, observed by the Chinese H $\alpha$  Solar Explorer (CHASE/HIS; [110, 111]), the initial magnetic field was provided by a NLFFF model with a multi-step construction procedure. In the first step, an SDO/HMI vector magnetogram was pre-processed to ensure that the photospheric magnetic field agrees with the NLFFF model assumptions in the local Cartesian coordinate system. In the second step, the MF in MPI-AMRVAC was applied and succeeded in producing an excellent initial condition for the MHD simulation of the eruption (Figures 1 panel a and d).

## 2.4 Magnetic flux ropes

With the NLFFF extrapolations, it is not apparent that bundles of highly twisted magnetic field lines can be obtained that prove the existence of a flux rope. Magnetic field lines may not show a flux rope but rather an arcade [8]. In these cases, flux ropes should be formed during the eruption process so they can be produced during the relaxation process.

For example, in the study of Prasad et al. [112], the MHD simulation starts with an extrapolated non-force-free magnetic field that is generated from a photospheric vector magnetogram of the concerned active region taken a few minutes before the onset of the flare. A sheared arcade is observed along the polarity inversion line in the magnetic topology before the flare. The shear created by the footpoints anchored in the photosphere initiates tether-cutting magnetic reconnection, which subsequently produces a flux rope above the flare arcade. The rising flux rope forms in a torus-unstable region, explaining the eruption. Similarly, Wang et al. [113] reproduced the formation of a pre-eruptive magnetic flux rope in NOAA 11429 and its eruption due to torus instability by implementing the photospheric velocity field. In another study, presented by Jiang et al. [57], after the analysis of the magnetic field topology, the transition from the pre-eruptive to the eruptive state is probably due to the upward expansion of internally stressed magnetic arcades of newly emerged flux reconnecting with external magnetic field which is the trigger of the eruption. The other possibility is that the coronal magnetic flux rope cannot be constructed well if the information is not correctly transformed from the bottom boundary to the coronal in weak fields. The NLFFF extrapolation is, in fact, an ill-posed problem [114]. To this end, the idea of incorporating the information from the coronal observations for reconstructing coronal magnetic fields is proposed. For example, a possibility is to insert a flux rope mimicking the shape of the eruptive filament as has been suggested already 20 years ago by van Ballegoijen [115], and as was more recently achieved [22, 62, 116–119]. In those cases, the relaxation can be done after the insertion of the flux tube.

In the study of Guo et al. [22] concerning the eruption of an H $\alpha$  filament observed by CHASE/HIS and the Atmosphere Imaging Assembly [AIA, 120] on board the Solar Dynamics Observatory (SDO), the potential field is first extrapolated using Green's function with the  $B_z$  component [78] after the pre-processing of a magnetogram. Then, the flux rope is superposed onto it. This flux rope is constructed with the Regularised

Biot-Savart laws (RBSLs; Titov et al. [121]). The RBSL method proposed by Titov et al. [121] can construct flux ropes with the axis of arbitrary path, which are more consistent with complicated flux rope proxies in observations. Based on this method, Guo et al. [22] construct the flux rope structure for a filament observed by CHASE (Figures 1a and 1d), in which the axis path, toroidal flux and cross-section radius of the RBSL flux rope are measured from observations. In their pipeline, the parameters of the RBSL flux rope are fully derived from or based on the observations. The flux rope path and its minor radius are approximated by the filament path and width [122], respectively, and the toroidal flux is approximated using the  $B_z$  map (refer to Guo et al. [47] for more details). They calculated the RBSL flux rope two times. The first time, they only computed the bottom boundary to prepare the boundary condition of the potential field extrapolation to keep the consistency of the superposed magnetic fields with the observed magnetogram. The second time is to compute the 3D distribution of the RBSL flux-rope magnetic fields in constructing the NLFFF.

To not perturb the photospheric magnetic field by the insertion of the flux rope, Guo et al. [47, 123] subtracted the photospheric magnetic field of the RBSL flux rope from the observed  $B_z$  before extrapolating the potential field. The resulting superposed photospheric magnetic fields combine the potential and RBSL flux-rope magnetic fields and agree with the observed surface magnetic field. Finally, the magneto-frictional method relaxes this magnetic field to a force-free state. It is what has been done in recent studies [22, 47, 62, 124]. The flux rope evolving with time obtained by the subsequent MHD simulation can be compared with the evolution of the observed filament (Figure 4).

### 3 Thermodynamic MHD models

The zero- $\beta$  models and even the isothermal models cannot self-consistently synthesise the radiation from the density and temperature, and the results from these models are thus not directly comparable to EUV observations. Hence, data-driven thermodynamic MHD models need to be developed to a better insight into the nature of some emission structures like filaments, EUV waves, and coronal loops [62]. Recently, a solar flare and a CME have been reproduced by a data-based MHD model considering the non-adiabatic effects [125].

There are two types of models: data-driven and data-constrained. The initial magnetic field is usually reconstructed using the NLFFF or magnetostatic extrapolation method, and the photospheric or low-coronal boundary is fixed or provided by numerical extrapolations. In these cases, a pre-eruptive magnetic flux rope generally exists to generate solar eruptions, as shown in Guo et al. [123]. In real data-driven models, the long-term evolution of the active region is studied to model the flux rope's formation (see Section 4).

#### 3.1 MHD and thermodynamic equations

In two recent works, Guo et al. [62] and Guo et al. [22] perform thermodynamic simulations of the eruptive events on 28 October 2021 and 18 August 2022, respectively.

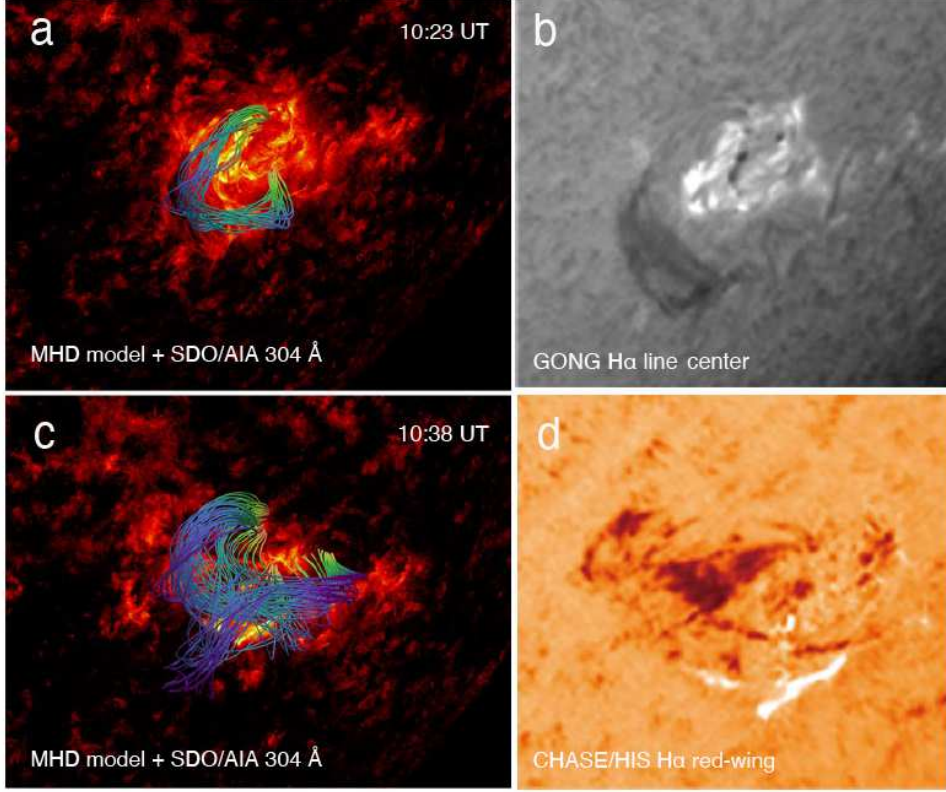


**Fig. 4** Comparison between the modelled flux rope and the filament observed in SDO/AIA 304 Å (Panels a and c), GONG H $\alpha$  line-centre (Panel b) and CHASE/HIS H $\alpha$  red-wing image (Panel d) (adapted from Guo et al. [22]).

In Guo et al. [62], they adopted a nonadiabatic MHD model that considers the field-aligned thermal conduction, empirical heating, and the optically thin radiation losses in the corona. The governing equations read as follows:

$$\frac{\partial \rho}{\partial t} + \nabla \cdot (\rho \mathbf{v}) = 0, \quad (3)$$

$$\frac{\partial (\rho \mathbf{v})}{\partial t} + \nabla \cdot (\rho \mathbf{v} \mathbf{v} + p_{tot} \mathbf{I} - \frac{\mathbf{B}\mathbf{B}}{\mu_0}) = \rho \mathbf{g}, \quad (4)$$

$$\frac{\partial \mathbf{B}}{\partial t} + \nabla \cdot (\mathbf{v}\mathbf{B} - \mathbf{B}\mathbf{v}) = 0, \quad (5)$$

$$\begin{aligned} \frac{\partial \varepsilon}{\partial t} + \nabla \cdot (\varepsilon \mathbf{v} + p_{tot} \mathbf{v} - \frac{\mathbf{B}\mathbf{B}}{\mu_0} \cdot \mathbf{v}) &= \rho \mathbf{g} \cdot \mathbf{v} + H_0 e^{-z/\lambda} - n_e n_H \Lambda(T) \\ + \nabla \cdot (\boldsymbol{\kappa} \cdot \nabla T), \end{aligned} \quad (6)$$

where  $p_{tot} \equiv p + B^2/(2\mu_0)$ , corresponds to the sum of the thermal pressure and the magnetic pressure,  $\mathbf{g} = -g_{\odot}r_{\odot}^2/(r_{\odot} + z)^2\mathbf{e}_z$  denotes the gravitational acceleration,  $g_{\odot} = 274 \text{ m s}^{-2}$  corresponds to the gravitational acceleration at the solar surface,  $r_{\odot}$  is the solar radius,  $\varepsilon = \rho v^2/2 + p/(\gamma - 1) + B^2/(2\mu_0)$  is the total energy density, the term  $\nabla \cdot (\boldsymbol{\kappa} \cdot \nabla T) = \nabla \cdot (\kappa_{\parallel} \hat{\mathbf{b}}\hat{\mathbf{b}} \cdot \nabla T)$  represents field-aligned thermal conduction,  $\kappa_{\parallel} = 10^{-6} T^{\frac{5}{2}} \text{ erg cm}^{-1} \text{ s}^{-1} \text{ K}^{-1}$  is the Spitzer heat conductivity,  $n_e n_H \Lambda(T)$  is the optically-thin radiative losses,  $H_0 e^{-z/\lambda}$  is an empirical heating to maintain the high temperature of the corona.

In these two papers, Guo et al. [22, 62] showed that the twisted flux rope and sheared field lines compare well with the observed filament and chromosphere fibrils. This indicates that the NLFFF model can serve as an initial condition for the MHD simulation, as shown in Figures 1a and 1d. The initial density and pressure then define a hydrostatic atmosphere from the chromosphere to the corona, which is described as follows:

$$T(z) = \begin{cases} T_{\text{ch}} + \frac{1}{2}(T_{\text{co}} - T_{\text{ch}})(\tanh(\frac{z-h_{\text{tr}}-0.27}{w_{\text{tr}}}) + 1) & z \leq h_{\text{tr}}, \\ (\frac{7}{2} \frac{F_c}{\kappa} (z - h_{\text{tr}}) + T_{\text{tr}}^{7/2})^{2/7} & z > h_{\text{tr}}, \end{cases} \quad (7)$$

where  $T_{\text{ch}} = 8000 \text{ K}$  corresponds to the chromospheric temperature,  $T_{\text{co}} = 1.5 \text{ MK}$  represents the coronal temperature,  $h_{\text{tr}} = 2 \text{ Mm}$  and  $w_{\text{tr}} = 0.2 \text{ Mm}$  control the height and thickness of initial transition region, and  $F_c = 2 \times 10^5 \text{ erg cm}^{-2} \text{ s}^{-1}$  is the constant thermal conduction flux. Hereafter, the density distribution is calculated from the number density at the bottom, i.e.,  $1.15 \times 10^{15} \text{ cm}^{-3}$ .

### 3.2 Case-studies of 28 October 2021 and 18 August 2022

For these two case studies, Guo et al. [22, 62] compared the results of the simulations to AIA observations. By including thermal conduction and radiative losses in the energy equation, they developed a novel data-driven thermodynamic magnetohydrodynamic model that can capture the thermodynamic evolution in contrast to the previous zero- $\beta$  model. Their numerical model reproduces multiple notable observational eruption features, incl. the erupted filament morphology, its path, and the flare ribbons. In the case of the event on 18 August 2022, the simulations indicate that magnetic reconnection of the flux-rope leg with the neighbouring sheared arcades may be the primary mechanism for the lateral drifting of filament materials. This also causes the flux-rope rotation [22]. This conduct agrees with the 3D *ar - rf* reconnection model [29]. They pointed out that the lateral drifting of filament materials can also serve as an observational signature for *ar - rf* reconnection, in addition to saddle-like flare loops [50] and the shift of filament legs [49]. They obtained synthesised images similar to the SDO/AIA observations (Figure 5).

Guo et al. [62] studied the 28 October 2021 event and reproduced the main observational characteristics of the X1.0 flare in NOAA active region 12887, starting with the morphology of the eruption and including the kinematics of the flare ribbons, the EUV emission, the CME [126], and even the two components of the EUV waves predicted by the magnetic stretching model of Chen et al. [127], namely a fast-mode

shock wave and a slower apparent wave which is due to consecutive magnetic field line stretching.

The simulation also reveals some fascinating phenomena. The flare ribbons initially separate and eventually stop at the outer stationary QSLs. These QSLs correspond to the borders of the filament channel and demarcate the flare ribbons' final positions. These, in turn, can be used to predict the lifetime and size of a flare before it occurs (Figure 6). Moreover, the side views of the synthesised EUV and white-light images display the typical three-part structure of CMEs. The bright leading front is approximately co-spatial with the EUV wave's non-wave component, which is in agreement with the previous observations [128]. These simulation results reinforce the effects of the magnetic field-line stretching model in explaining the slow component of EUV waves (Figure 7).

## 4 Long-term data-driven Models

Data-driven models are superior to data-constrained types. The corona responds to the photosphere in real time. Data-driven models are suitable for studying the long-term evolution of active regions.

The NOAA active region 12673 was the site of 4 X-ray class flares and many M-class flares in September 2017. The evolution of this active region and associated solar flares has been extensively investigated using numerical models [20, 129–131].

### 4.1 Case-study of 6 September 2017

In this review, we present the work of Guo et al. [101] and discuss the robustness of the proposed data-driven model. They developed a full data-driven model to study the long-term evolution of this active region and its produced confined X2.2 flare of 6 September 2017 (SOL2017-09-06T08:57), which occurred a few hours before the large X 9.3 flare in AR NOAA 12673. The question of the confinement of this flare was debated in Liu et al. [132]. At 09:48 UT, two bright points are visible in the inner part of LASCO/C2 and develop as faint coronal flows. However, several points show that these coronal flows do not correspond to a CME expelled from the active region: the non-lateral extension of flare ribbons and the non-visibility of dimmings, and finally, the velocity estimated from the duration between the flare onset and observed CME is larger than that of this coronal flow. On the contrary, the second flare X9.3 presents the former characteristics and is very eruptive [58].

In this data-driven modelling, the initial magnetic field is the potential field model, and the bottom boundary is provided by the time series of the observed vector magnetograms during one day and derived DAVE4VM velocity fields. 300 vector magnetograms have been used for this study. As a result, the bottom boundaries of the simulation are synchronised with the observations at every computation time step. In the data-constrain models used for the case studies of 28 October 2021 and 18 August 2022, the initial magnetic field is provided by the NLFFF extrapolation of one vector magnetogram and the incorporation of flux ropes; the driven duration is within 2 hours until the eruption. In the full data-driven model proposed in Guo et al. [101] the flux rope is not incorporated but formed through the long-term evolution of the

active region. The final state of the time-dependent magnetofrictional (TMF) modelling further serves as the initial prerequisite for the thermodynamic MHD simulation, enabling us to investigate the formation and eruption of the observed flux rope.

They employ a data-driven technique to study the flux rope’s entire process, from its birth to its eruption. The initial magnetic field, before the eruption, is a potential field, and the subsequent coronal evolution is entirely influenced by the observational HMI magnetograms in the photosphere via the TMF approach. Figure 8 illustrates the evolution of the 3D coronal magnetic fields and the comparisons with the SDO/AIA 304 Å observations. It is found that the flux rope formed consistently by coupling the TMF approach with the thermodynamic MHD model [101]. The magnetic topology properties of the simulated flux rope are shown in Figure 9, from which one can see that the twist numbers of certain flux-rope field lines are more significant than one and are recognised as the quasi-circular QSLs. Figure 10 reveals the transformation from sheared arcades (Figure 10a) to the flux rope that is well comparable to the observed hot channel in SDO/AIA 131 Å wavelength (Figure 10b), which is formed due to flux cancellation driven by collisional shearing motions (Figure 10c). Additionally, it is also found there exists a current sheet represented by a high  $J/B$  region, where the traced field lines are composed of two groups of sheared arcades and the central twisted flux rope, as shown in Figure 10d. This data-driven model validates the effectiveness of collisional shearing motions in forming flux ropes in complicated active regions [133].

## 4.2 Comparison with other data-driven models

With the development of observational instruments and numerical techniques, the data-driven MHD simulations have become one novel and advanced method to reconstruct the time-evolving solar corona and, therefore, unveil the underlying physics behind observations. The treatments of governing equations and boundaries are different in various data-driven models. Regarding the governing equation, the models can be divided into TMF model [63, 64, 98], zero- $\beta$  [47, 56, 61, 123, 134], isothermal [57, 58, 135], thermodynamic MHD [22, 62], and the hybrid models [66, 101, 136]. Among them, the evolution of the TMF model is assumed to be quasi-static such that it is pretty suitable to reproduce the long-term evolution of active regions and the flux rope formation at a fast speed. The zero- $\beta$  and isothermal MHD models omit the thermodynamic evolution of the plasma while capturing the rapid evolution of 3D coronal magnetic fields. The thermodynamic data-driven MHD model is more advanced and is capable of retrieving the evolution of magnetic topology evolution and thermodynamics, as shown in Guo et al. [62]. The data-driven boundaries can be classified into the  $B$  or  $v - B$  [47, 57],  $v$  [46, 61, 113] and  $E$  [63, 64] driven boundaries. Each of these boundary conditions has its own advantages in physics and numerical schemes. For example,  $B$ -driven boundary can reproduce the evolution of vector magnetic fields in observations by replacing a time series of observed magnetograms. However, this option will also introduce numerical magnetic-field divergence induced by the driven boundary. In contrast,  $E$ -driven and  $V$ -driven boundaries can better address such numerical issues, although they strongly rely on the inversion method: deriving the velocity fields or electric fields capable of retrieving the evolution of magnetic fields in observations. To this end, several numerical approaches have

been proposed, such as the well-known DAVE4VM method [137] for deriving photospheric flows, and the PDFLSS method for deriving both inductive and non-inductive electric fields [65]. Welsch et al. [138] discussed comparisons of different inversion techniques for photospheric flows. Wang et al. [139] compared the effects of two types of derived photospheric flows with data-driven MHD simulations. Notably,  $E$ -driven and  $V$ -driven boundaries can be effectively coupled with the advanced CT method, ensuring that the divergence of magnetic fields introduced during numerical computation is controlled to the magnitude of machine precision. Toriumi et al. [140] compared the ability of the well-known data-driven models to reproduce the solar eruption in a flux emergence simulation. The differences induced by adopted physical models and data-driven boundaries are worth doing in future works.

As previously mentioned, several numerical MHD models have been used to investigate the evolution of the active region (AR NOAA 12673). The associated solar flares, particularly the second X-ray flare, were eruptive [20, 129–131]. Therefore, to evaluate the usefulness of the novel data-driven model [101] to reproduce the observations concerning these long lists of models, one must conduct a comparison between the new simulation results and previous results. The comparison can be conducted from various aspects, including the typical magnetic topology, magnetic relative helicity and energy budgets. Firstly, the results of Guo et al. [101] exhibit similar trends and magnitudes in magnetic helicity and energy budgets to the TMF simulation carried out by Price et al. [130] for the same active region. A similarity in the ratio between the current-carrying helicity and total helicity by September 2017 is noted, approximately at 0.15, though the ratio between magnetic free energy to total magnetic energy in Guo et al. [101] is slightly higher. This discrepancy could be attributed to different initial conditions (such as the starting time of the potential field extrapolation) and the driven boundary conditions ( $E$  or  $v - B$ ). Regarding the magnetic topology, many papers focusing on modelling this active region identify two null-point reconnection sites at the onset of eruption [130, 131, 136, 141, 142]. This consistency with previous findings validates the robustness of the data-driven model of Guo et al. [101] in reproducing observed solar eruptions.

The hybrid model combined with TMF and thermodynamic MHD modellings in Guo et al. [101] presents several advances, enabling it to capture both the long-term buildup and subsequent drastic release of magnetic energy with a rapid computation speed. However, this operation could trigger a numerical eruption. On the one hand, the system may undergo a non-smooth transition when switching from the TMF model to the MHD model, such that the selection of the switching time is crucial for the trigger of eruptions, as demonstrated in Daei et al. [136]. On the other hand, the final magnetic-field state in the TMF model generally cannot perfectly satisfy the force-free condition. As a result, the nontrivial residual Lorentz force may lead to the ascent of the flux rope formed in the TMF model Afanasyev et al. [66]. Therefore, to study the initiation process of a CME, such as the slow-rise phase and the trigger [30], the MHD model going through the entire process from formation to eruption of a CME flux rope is more suitable, as done in Jiang et al. [135].

## 5 Confined/eruptive event: conditions

Theories on eruption mechanisms have also advanced in recent years. The existing models can be divided into two types. The first type is based on magnetic reconnection occurring at high-lying null point [143]. The reconnection of the overlying magnetic field lines leads to a breakout [44]. When the magnetic strength is too strong, the flux rope is trapped in a magnetic cage and cannot erupt [144]. The orientation of the magnetic field at the top of the flux rope with the environment can lead to confined eruptive eruptions depending on the parallel or anti-parallel lines [145]. A rotation of the flux rope could lead to such a configuration and finally to a confined eruption [146, 147]. The reconnection may also occur below the flux rope, corresponding to the tether-cutting mechanism model [90]. In this model, new flux can be injected, providing an upward Lorentz force to the erupting structure [148].

The second type is based on ideal magnetohydrodynamic (MHD) instabilities, e.g., the helical kink instability [149] or the torus instability [41, 43]. The torus instability can trigger a flux rope eruption [47].

The torus instability is mainly dominated by the hoop force  $F_H$  and the strapping force  $F_s$ . The threshold of the eruptive event is given by the decay index of the background strapping fields ( $n > 1.5$ ) but can be less or more [87, 150, 151], for the following reasons. On the one hand, the threshold of the decay index is related to the aspect ratio of the flux rope. For example, Démoulin and Aulanier [150] found that the threshold of the decay index decreases to a value of 1.1 for the thick current. On the other hand, other than the strapping force induced by the poloidal magnetic fields, the toroidal-field tension force [152, 153], and the force resulting from the non-axisymmetry of the flux rope can also suppress the rising of the flux rope [56].

The previous sections have shown that thermodynamic magnetohydrodynamic simulations with refined treatments on the active region evolution and energy transfer have been greatly developed. These enable us to better understand the trigger of flux rope eruption. In such simulations, the magnetic field and coronal plasma evolve fully self-consistently. The simulations provide synthetic images that can be compared with remote-sensing observations of different spacecraft and the values of physical parameters in 3D. Therefore, the causes of eruption or confinement can be described by the involved forces [101, 154, 155].

Guo et al. [101] unveils the nature of the confined X2.2 eruption on 6 September 2017 with a data-driven simulation. They found that the rotation of the flux rope can lead to the transformation of the overlying magnetic fields from the poloidal to the toroidal direction, thereby increasing the toroidal tension force while decreasing the poloidal strapping force. This is also mentioned in Zhong et al. [134]. Figure 11 exhibits the Lorentz force involved in the flux rope ejections, including the net Lorentz force ( $F_L$ ), the hoop force ( $F_H$ ) and strapping force ( $F_S$ ) and the tension force ( $F_T$ ). As illustrated in Figure 11d, the rising of the flux rope is dominantly constrained by the tension force. More intriguingly, Zhang et al. [156] studied the constraints of a failed filament eruption associated with the large-angle rotation. They found that the direction of the strapping force becomes upward after the flux-rope rotation that is larger than  $90^\circ$ , meaning that the poloidal-field strapping force cannot serve as the constraints for the eruption events with the large-angle rotation. This also



self-consistently explains why so many failed filament eruptions with the large-angle rotation are torus-unstable [146]. Figure 12 provided a sketch to show a failed eruption constrained by the tension force induced by overlying toroidal magnetic fields [155].

It should be noted that the effects of the tension force in constraining solar eruptions have also previously been found in observations [157]. They computed the three components of the magnetic fields directly derived from the PFSS model and demonstrated that the tension force was more significant above the active region and led to a confined flare [157].

## 6 Conclusion

In this paper, we have reviewed a few advanced numerical MHD simulations concerning solar eruptions. All of them include two steps: modelling setup and numerical solving of MHD equations. In the setup stage, the primary input is the 3D magnetic fields as the initial condition, which can be provided by the potential field model or the results reconstructed from the NLFFF extrapolation. The bottom boundaries are constrained or driven by observed vector magnetograms and photospheric flows.

1. If we aim to investigate the accumulation process of magnetic free energy and helicity, the potential field should establish the initial coronal magnetic field in data-driven models. The coronal magnetic fields become sheared and twisted, driven by input data-driven boundaries such as the vector magnetograms and photospheric flows. In addition, the starting point of the simulation should be a time when the field is close to the potential field, far from the onset time of the eruption.
2. If we mainly talk about the eruption process rather than studying the established method of the eruptive flux rope, the initial magnetic fields can be directly provided by the NLFFF extrapolation. In this case, the core fields for the eruption, such as flux ropes, could be included in the NLFFF extrapolation, namely, the initial magnetic field condition for the subsequent MHD simulation. The magneto-frictional relaxation combined with the RBSL flux-rope insertion is just used to construct the NLFFF, which is adopted in Guo et al. [22, 62, 123].
3. More recently has been developed a global coronal model (COCONUT- Perri et al. [158, 159]), where a realistic solar wind reconstructed from observed magnetograms is superposed in the corona [25, 26]. The implementation of the RBSL flux rope model in COCONUT is promising and can be coupled to EUHFORIA simulations to predict space weather events in the Earth's environment [160, 161].

These new thermodynamic data-driven MHD simulations allow us to understand eruptions and the forces involved in confined or eruptive events. They follow the actual Sun and open a new domain of research, which leads to better predictions of eruptive phenomena and partition of the release of magnetic energy in the atmosphere.

**Acknowledgements.** These results were also obtained in the framework of the projects C14/19/089 (C1 project Internal Funds KU Leuven), G0B5823N and G002523N (WEAVE) (FWO-Vlaanderen), 4000134474 (SIDC Data Exploitation, ESA Prodex), and Belspo project B2/191/P1/SWiM. For the computations, we used the

VSC—Flemish Supercomputer Center infrastructure, funded by the Hercules Foundation and the Flemish Government Department EWI. BS wants to thank FWO for supporting her trip to Nagoya for the 7th Asia-Pacific Conference on Plasma Physics from November 12 to 17, where she presented this review. We are indebted to Luis Linan for his fruitful comments on this review.

## References

- [1] Green, L.M., Kliem, B., Wallace, A.J.: Photospheric flux cancellation and associated flux rope formation and eruption. *A&A* **526**, 2 (2011) <https://doi.org/10.1051/0004-6361/201015146> [arXiv:1011.1227](https://arxiv.org/abs/1011.1227) [astro-ph.SR]
- [2] Cheng, X., Zhang, J., Liu, Y., Ding, M.D.: Observing Flux Rope Formation During the Impulsive Phase of a Solar Eruption. *ApJ letters* **732**(2), 25 (2011) <https://doi.org/10.1088/2041-8205/732/2/L25> [arXiv:1103.5084](https://arxiv.org/abs/1103.5084) [astro-ph.SR]
- [3] Schmieder, B., Démoulin, P., Aulanier, G.: Solar filament eruptions and their physical role in triggering coronal mass ejections. *Advances in Space Research* **51**(11), 1967–1980 (2013) <https://doi.org/10.1016/j.asr.2012.12.026> [arXiv:1212.4014](https://arxiv.org/abs/1212.4014) [astro-ph.SR]
- [4] Cheng, X., Ding, M.D.: The Characteristics of the Footpoints of Solar Magnetic Flux Ropes during Eruptions. *ApJ supplement* **225**(1), 16 (2016) <https://doi.org/10.3847/0067-0049/225/1/16> [arXiv:1605.04047](https://arxiv.org/abs/1605.04047) [astro-ph.SR]
- [5] Zurbuchen, T.H., Richardson, I.G.: In-Situ Solar Wind and Magnetic Field Signatures of Interplanetary Coronal Mass Ejections. *Space Science Reviews* **123**(1-3), 31–43 (2006) <https://doi.org/10.1007/s11214-006-9010-4>
- [6] Duan, A., Jiang, C., He, W., Feng, X., Zou, P., Cui, J.: A Study of Pre-flare Solar Coronal Magnetic Fields: Magnetic Flux Ropes. *ApJ* **884**(1), 73 (2019) <https://doi.org/10.3847/1538-4357/ab3e33> [arXiv:1908.08643](https://arxiv.org/abs/1908.08643) [astro-ph.SR]
- [7] Maharana, A., Isavnin, A., Scolini, C., Wijsen, N., Rodriguez, L., Mierla, M., Magdalenic, J., Poedts, S.: Implementation and validation of the FRi3D flux rope model in EUHFORIA. *Advances in Space Research* **70**(6), 1641–1662 (2022) <https://doi.org/10.1016/j.asr.2022.05.056> [arXiv:2207.06707](https://arxiv.org/abs/2207.06707) [astro-ph.SR]
- [8] Guo, Y., Schmieder, B., Démoulin, P., Wiegmann, T., Aulanier, G., Török, T., Bommier, V.: Coexisting Flux Rope and Dipped Arcade Sections Along One Solar Filament. *ApJ* **714**(1), 343–354 (2010) <https://doi.org/10.1088/0004-637X/714/1/343>
- [9] Zhou, G.P., Zhang, J., Wang, J.X.: Observations of Magnetic Flux-rope Oscillation during the Precursor Phase of a Solar Eruption. *ApJ letters* **823**(1), 19 (2016) <https://doi.org/10.3847/2041-8205/823/1/L19>

- [10] Syntelis, P., Gontikakis, C., Patsourakos, S., Tsinganos, K.: The spectroscopic imprint of the pre-eruptive configuration resulting into two major coronal mass ejections. *A&A* **588**, 16 (2016) <https://doi.org/10.1051/0004-6361/201526829> [arXiv:1602.03680](https://arxiv.org/abs/1602.03680) [astro-ph.SR]
- [11] Joshi, N.C., Sterling, A.C., Moore, R.L., Magara, T., Moon, Y.-J.: Onset of a Large Ejective Solar Eruption from a Typical Coronal-jet-base Field Configuration. *ApJ* **845**(1), 26 (2017) <https://doi.org/10.3847/1538-4357/aa7c1b> [arXiv:1706.09176](https://arxiv.org/abs/1706.09176) [astro-ph.SR]
- [12] Chen, P.F., Innes, D.E., Solanki, S.K.: SOHO/SUMER observations of prominence oscillation before eruption. *A&A* **484**(2), 487–493 (2008) <https://doi.org/10.1051/0004-6361:200809544> [arXiv:0802.1961](https://arxiv.org/abs/0802.1961) [astro-ph]
- [13] Ni, L., Chen, Y., Peter, H., Tian, H., Lin, J.: A magnetic reconnection model for hot explosions in the cool atmosphere of the Sun. *A&A* **646**, 88 (2021) <https://doi.org/10.1051/0004-6361/202039239> [arXiv:2011.07692](https://arxiv.org/abs/2011.07692) [astro-ph.SR]
- [14] Cheng, X., Xing, C., Aulanier, G., Solanki, S.K., Peter, H., Ding, M.D.: Deciphering the Slow-rise Precursor of a Major Coronal Mass Ejection. *ApJ letters* **954**(2), 47 (2023) <https://doi.org/10.3847/2041-8213/acf3e4> [arXiv:2308.13136](https://arxiv.org/abs/2308.13136) [astro-ph.SR]
- [15] Cheng, X., Zhang, J., Liu, Y., Ding, M.D.: Observing Flux Rope Formation During the Impulsive Phase of a Solar Eruption. *ApJ letters* **732**(2), 25 (2011) <https://doi.org/10.1088/2041-8205/732/2/L25> [arXiv:1103.5084](https://arxiv.org/abs/1103.5084) [astro-ph.SR]
- [16] Zhang, J., Cheng, X., Ding, M.-D.: Observation of an evolving magnetic flux rope before and during a solar eruption. *Nature Communications* **3**, 747 (2012) <https://doi.org/10.1038/ncomms1753> [arXiv:1203.4859](https://arxiv.org/abs/1203.4859) [astro-ph.SR]
- [17] Webb, D.F.: Understanding CMEs and their source regions. *Journal of Atmospheric and Solar-Terrestrial Physics* **62**(16), 1415–1426 (2000) [https://doi.org/10.1016/S1364-6826\(00\)00075-4](https://doi.org/10.1016/S1364-6826(00)00075-4)
- [18] Guo, Y., Ding, M.D., Cheng, X., Zhao, J., Pariat, E.: Twist Accumulation and Topology Structure of a Solar Magnetic Flux Rope. *ApJ* **779**(2), 157 (2013) <https://doi.org/10.1088/0004-637X/779/2/157> [arXiv:1311.1883](https://arxiv.org/abs/1311.1883) [astro-ph.SR]
- [19] Pariat, E., Leake, J.E., Valori, G., Linton, M.G., Zuccarello, F.P., Dalmasse, K.: Relative magnetic helicity as a diagnostic of solar eruptivity. *A&A* **601**, 125 (2017) <https://doi.org/10.1051/0004-6361/201630043> [arXiv:1703.10562](https://arxiv.org/abs/1703.10562) [astro-ph.SR]
- [20] Moraitis, K., Sun, X., Pariat, É., Linan, L.: Magnetic helicity and eruptivity in active region 12673. *A&A* **628**, 50 (2019) <https://doi.org/10.1051/0004-6361/201935870> [arXiv:1907.06365](https://arxiv.org/abs/1907.06365) [astro-ph.SR]

- [21] Kusano, K., Iju, T., Bamba, Y., Inoue, S.: A physics-based method that can predict imminent large solar flares. *Science* **369**(6503), 587–591 (2020) <https://doi.org/10.1126/science.aaz2511>
- [22] Guo, J.H., Qiu, Y., Ni, Y.W., Guo, Y., Li, C., Gao, Y.H., Schmieder, B., Poedts, S., Chen, P.F.: Understanding the Lateral Drifting of an Erupting Filament with a Data-constrained Magnetohydrodynamic Simulation. *ApJ* **956**(2), 119 (2023) <https://doi.org/10.3847/1538-4357/acf198> [arXiv:2308.08831](https://arxiv.org/abs/2308.08831) [astro-ph.SR]
- [23] Guo, Y., Zhong, Z., Ding, M.D., Chen, P.F., Xia, C., Keppens, R.: Data-constrained Magnetohydrodynamic Simulation of a Long-duration Eruptive Flare. *ApJ* **919**(1), 39 (2021) <https://doi.org/10.3847/1538-4357/ac10c8> [arXiv:2106.15080](https://arxiv.org/abs/2106.15080) [astro-ph.SR]
- [24] Cheng, X., Zhang, J., Ding, M.D., Liu, Y., Poomvises, W.: The Driver of Coronal Mass Ejections in the Low Corona: A Flux Rope. *ApJ* **763**(1), 43 (2013) <https://doi.org/10.1088/0004-637X/763/1/43> [arXiv:1211.6524](https://arxiv.org/abs/1211.6524) [astro-ph.SR]
- [25] Guo, J., Linan, L., Poedts, S., Guo, Y., Lani, A., Schmieder, B., Brchnelova, M., Perri, B., Baratashvili, T., Ni, Y., *et al.*: Modeling the propagation of coronal mass ejections with coconut: Implementation of the regularized biot-savart law flux rope model. *A&A* **683**, 54 (2024)
- [26] Linan, L., Regnault, F., Perri, B., Brchnelova, M., Kuzma, B., Lani, A., Poedts, S., Schmieder, B.: Self-consistent propagation of flux ropes in realistic coronal simulations. *A&A* **675**, 101 (2023) <https://doi.org/10.1051/0004-6361/202346235> [arXiv:2305.02089](https://arxiv.org/abs/2305.02089) [astro-ph.SR]
- [27] Aulanier, G., Pariat, E., Démoulin, P.: Current sheet formation in quasi-separatrix layers and hyperbolic flux tubes. *A&A* **444**(3), 961–976 (2005) <https://doi.org/10.1051/0004-6361:20053600>
- [28] Janvier, M., Aulanier, G., Bommier, V., Schmieder, B., Démoulin, P., Pariat, E.: Electric Currents in Flare Ribbons: Observations and Three-dimensional Standard Model. *ApJ* **788**(1), 60 (2014) <https://doi.org/10.1088/0004-637X/788/1/60> [arXiv:1402.2010](https://arxiv.org/abs/1402.2010) [astro-ph.SR]
- [29] Aulanier, G., Dudík, J.: Drifting of the line-tied footpoints of CME flux-rope. *A&A* **621**, 72 (2019) <https://doi.org/10.1051/0004-6361/201834221> [arXiv:1811.04253](https://arxiv.org/abs/1811.04253) [astro-ph.SR]
- [30] Xing, C., Aulanier, G., Cheng, X., Xia, C., Ding, M.: Unveiling the Initiation Route of Coronal Mass Ejections through their Slow Rise Phase. *arXiv e-prints*, 2402–16679 (2024) <https://doi.org/10.48550/arXiv.2402.16679> [arXiv:2402.16679](https://arxiv.org/abs/2402.16679) [astro-ph.SR]
- [31] Carmichael, H.: A Process for Flares. In: NASA Special Publication vol. 50, p.

451 (1964)

- [32] Sturrock, P.A., Coppi, B.: A New Model of Solar Flares. *ApJ* **143**, 3 (1966) <https://doi.org/10.1086/148472>
- [33] Hirayama, T.: Theoretical Model of Flares and Prominences. I: Evaporating Flare Model. *Solar Physics* **34**(2), 323–338 (1974) <https://doi.org/10.1007/BF00153671>
- [34] Kopp, R., Pneuman, G.W.: Nonstationary flow resulting from field line reconnection following a major coronal transient. In: *Bulletin of the American Astronomical Society*, vol. 8, p. 293 (1976)
- [35] Lin, J., Forbes, T.G.: Effects of reconnection on the coronal mass ejection process. *JGR* **105**(A2), 2375–2392 (2000) <https://doi.org/10.1029/1999JA900477>
- [36] Priest, E.R., Démoulin, P.: Three-dimensional magnetic reconnection without null points. 1. Basic theory of magnetic flipping. *JGR* **100**(A12), 23443–23464 (1995) <https://doi.org/10.1029/95JA02740>
- [37] Janvier, M., Aulanier, G., Pariat, E., Démoulin, P.: The standard flare model in three dimensions. III. Slip-running reconnection properties. *A&A* **555**, 77 (2013) <https://doi.org/10.1051/0004-6361/201321164> [arXiv:1305.4053](https://arxiv.org/abs/1305.4053) [astro-ph.SR]
- [38] Demoulin, P., Henoux, J.C., Priest, E.R., Mandrini, C.H.: Quasi-Separatrix layers in solar flares. I. Method. *A&A* **308**, 643–655 (1996)
- [39] Titov, V.S., Hornig, G., Démoulin, P.: Theory of magnetic connectivity in the solar corona. *Journal of Geophysical Research (Space Physics)* **107**(A8), 1164 (2002) <https://doi.org/10.1029/2001JA000278>
- [40] Zhao, J., Li, H., Pariat, E., Schmieder, B., Guo, Y., Wiegmann, T.: Temporal Evolution of the Magnetic Topology of the NOAA Active Region 11158. *ApJ* **787**(1), 88 (2014) <https://doi.org/10.1088/0004-637X/787/1/88> [arXiv:1404.5004](https://arxiv.org/abs/1404.5004) [astro-ph.SR]
- [41] Aulanier, G., Török, T., Démoulin, P., DeLuca, E.E.: Formation of Torus-Unstable Flux Ropes and Electric Currents in Erupting Sigmoids. *ApJ* **708**(1), 314–333 (2010) <https://doi.org/10.1088/0004-637X/708/1/314>
- [42] Amari, T., Luciani, J.F., Aly, J.J., Mikic, Z., Linker, J.: Coronal Mass Ejection: Initiation, Magnetic Helicity, and Flux Ropes. I. Boundary Motion-driven Evolution. *ApJ* **585**(2), 1073–1086 (2003) <https://doi.org/10.1086/345501>
- [43] Kliem, B., Török, T.: Torus Instability. *PRL* **96**(25), 255002 (2006) <https://doi.org/10.1103/PhysRevLett.96.255002> [arXiv:physics/0605217](https://arxiv.org/abs/physics/0605217) [physics.plasm-ph]
- [44] Antiochos, S.K., DeVore, C.R., Klimchuk, J.A.: A Model for Solar Coronal

- Mass Ejections. *ApJ* **510**(1), 485–493 (1999) <https://doi.org/10.1086/306563> [arXiv:astro-ph/9807220](https://arxiv.org/abs/astro-ph/9807220) [astro-ph]
- [45] Schmieder, B., Demoulin, P., Aulanier, G., Golub, L.: Differential Magnetic Field Shear in an Active Region. *ApJ* **467**, 881 (1996) <https://doi.org/10.1086/177662>
- [46] Jiang, C., Feng, X., Liu, R., Yan, X., Hu, Q., Moore, R.L., Duan, A., Cui, J., Zuo, P., Wang, Y., Wei, F.: A fundamental mechanism of solar eruption initiation. *Nature Astronomy* **5**, 1126–1138 (2021) <https://doi.org/10.1038/s41550-021-01414-z> [arXiv:2107.08204](https://arxiv.org/abs/2107.08204) [astro-ph.SR]
- [47] Guo, Y., Xia, C., Keppens, R., Ding, M.D., Chen, P.F.: Solar Magnetic Flux Rope Eruption Simulated by a Data-driven Magnetohydrodynamic Model. *ApJ Letters* **870**(2), 21 (2019) <https://doi.org/10.3847/2041-8213/aafabf> [arXiv:1812.10030](https://arxiv.org/abs/1812.10030) [astro-ph.SR]
- [48] Chen, P.F., Shibata, K.: An Emerging Flux Trigger Mechanism for Coronal Mass Ejections. *ApJ* **545**(1), 524–531 (2000) <https://doi.org/10.1086/317803>
- [49] Dudík, J., Lörinčík, J., Aulanier, G., Zemanová, A., Schmieder, B.: Observation of All Pre- and Post-reconnection Structures Involved in Three-dimensional Reconnection Geometries in Solar Eruptions. *ApJ* **887**(1), 71 (2019) <https://doi.org/10.3847/1538-4357/ab4f86> [arXiv:1910.08620](https://arxiv.org/abs/1910.08620) [astro-ph.SR]
- [50] Lörinčík, J., Dudík, J., Aulanier, G.: Saddle-shaped Solar Flare Arcades. *ApJ letters* **909**(1), 4 (2021) <https://doi.org/10.3847/2041-8213/abe7f7> [arXiv:2102.10858](https://arxiv.org/abs/2102.10858) [astro-ph.SR]
- [51] Xing, C., Cheng, X., Ding, M.D.: Evolution of the Toroidal Flux of CME Flux Ropes during Eruption. *The Innovation* **1**(3), 100059 (2020) <https://doi.org/10.1016/j.xinn.2020.100059> [arXiv:2011.10750](https://arxiv.org/abs/2011.10750) [astro-ph.SR]
- [52] Aulanier, G., Démoulin, P., Schrijver, C.J., Janvier, M., Pariat, E., Schmieder, B.: The standard flare model in three dimensions. II. Upper limit on solar flare energy. *A&A* **549**, 66 (2013) <https://doi.org/10.1051/0004-6361/201220406> [arXiv:1212.2086](https://arxiv.org/abs/1212.2086) [astro-ph.SR]
- [53] Kliem, B., Su, Y.N., van Ballegooijen, A.A., DeLuca, E.E.: Magnetohydrodynamic Modeling of the Solar Eruption on 2010 April 8. *ApJ* **779**(2), 129 (2013) <https://doi.org/10.1088/0004-637X/779/2/129> [arXiv:1304.6981](https://arxiv.org/abs/1304.6981) [astro-ph.SR]
- [54] Inoue, S., Shiota, D., Bamba, Y., Park, S.-H.: Magnetohydrodynamic Modeling of a Solar Eruption Associated with an X9.3 Flare Observed in the Active Region 12673. *ApJ* **867**(1), 83 (2018) <https://doi.org/10.3847/1538-4357/aae079> [arXiv:1809.02309](https://arxiv.org/abs/1809.02309) [astro-ph.SR]
- [55] Amari, T., Canou, A., Aly, J.-J., Delyon, F., Alauzet, F.: Magnetic cage and

- rope as the key for solar eruptions. *Nature* **554**(7691), 211–215 (2018) <https://doi.org/10.1038/nature24671>
- [56] Zhong, Z., Guo, Y., Ding, M.D.: The role of non-axisymmetry of magnetic flux rope in constraining solar eruptions. *Nature Communications* **12**, 2734 (2021) <https://doi.org/10.1038/s41467-021-23037-8> arXiv:2105.07339 [astro-ph.SR]
- [57] Jiang, C., Wu, S.T., Yurchyshyn, V., Wang, H., Feng, X., Hu, Q.: How Did a Major Confined Flare Occur in Super Solar Active Region 12192? *ApJ* **828**(1), 62 (2016) <https://doi.org/10.3847/0004-637X/828/1/62> arXiv:1606.09334 [astro-ph.SR]
- [58] Jiang, C., Zou, P., Feng, X., Hu, Q., Liu, R., Vemareddy, P., Duan, A., Zuo, P., Wang, Y., Wei, F.: Magnetohydrodynamic Simulation of the X9.3 Flare on 2017 September 6: Evolving Magnetic Topology. *ApJ* **869**(1), 13 (2018) <https://doi.org/10.3847/1538-4357/aaeacc> arXiv:1810.13095 [astro-ph.SR]
- [59] Jiang, C., Feng, X., Guo, Y., Hu, Q.: Data-driven modeling of solar coronal magnetic field evolution and eruptions. *The Innovation* **3**, 100236 (2022) <https://doi.org/10.1016/j.xinn.2022.100236>
- [60] Hayashi, K., Feng, X., Xiong, M., Jiang, C.: An MHD Simulation of Solar Active Region 11158 Driven with a Time-dependent Electric Field Determined from HMI Vector Magnetic Field Measurement Data. *ApJ* **855**(1), 11 (2018) <https://doi.org/10.3847/1538-4357/aaacd8>
- [61] Kaneko, T., Park, S.-H., Kusano, K.: Data-driven MHD Simulation of Successive Solar Plasma Eruptions. *ApJ* **909**(2), 155 (2021) <https://doi.org/10.3847/1538-4357/abe414> arXiv:2101.12395 [astro-ph.SR]
- [62] Guo, J.H., Ni, Y.W., Zhong, Z., Guo, Y., Xia, C., Li, H.T., Poedts, S., Schmieder, B., Chen, P.F.: Thermodynamic and Magnetic Topology Evolution of the X1.0 Flare on 2021 October 28 Simulated by a Data-driven Radiative Magnetohydrodynamic Model. *ApJS* **266**(1), 3 (2023) <https://doi.org/10.3847/1538-4365/acc797> arXiv:2303.13980 [astro-ph.SR]
- [63] Cheung, M.C.M., DeRosa, M.L.: A Method for Data-driven Simulations of Evolving Solar Active Regions. *ApJ* **757**(2), 147 (2012) <https://doi.org/10.1088/0004-637X/757/2/147> arXiv:1208.2954 [astro-ph.SR]
- [64] Pomoell, J., Lumme, E., Kilpua, E.: Time-dependent Data-driven Modeling of Active Region Evolution Using Energy-optimized Photospheric Electric Fields. *Solar Physics* **294**(4), 41 (2019) <https://doi.org/10.1007/s11207-019-1430-x>
- [65] Fisher, G.H., Kazachenko, M.D., Welsch, B.T., Sun, X., Lumme, E., Bercik, D.J., DeRosa, M.L., Cheung, M.C.M.: The PDFLSS Electric Field Inversion Software. *ApJS* **248**(1), 2 (2020) <https://doi.org/10.3847/1538-4365/ab8303>

[arXiv:1912.08301](https://arxiv.org/abs/1912.08301) [astro-ph.SR]

- [66] Afanasyev, A.N., Fan, Y., Kazachenko, M.D., Cheung, M.C.M.: Hybrid Data-driven Magnetofrictional and Magnetohydrodynamic Simulations of an Eruptive Solar Active Region. *ApJ* **952**(2), 136 (2023) <https://doi.org/10.3847/1538-4357/acd7e9> [arXiv:2306.05388](https://arxiv.org/abs/2306.05388) [astro-ph.SR]
- [67] Scherrer, P.H., Bogart, R.S., Bush, R.I., Hoeksema, J.T., Kosovichev, A.G., Schou, J., Rosenberg, W., Springer, L., Tarbell, T.D., Title, A., Wolfson, C.J., Zayer, I., MDI Engineering Team: The Solar Oscillations Investigation - Michelson Doppler Imager. *Solar Physics* **162**(1-2), 129–188 (1995) <https://doi.org/10.1007/BF00733429>
- [68] Scherrer, P.H., Schou, J., Bush, R.I., Kosovichev, A.G., Bogart, R.S., Hoeksema, J.T., Liu, Y., Duvall, T.L., Zhao, J., Title, A.M., Schrijver, C.J., Tarbell, T.D., Tomczyk, S.: The Helioseismic and Magnetic Imager (HMI) Investigation for the Solar Dynamics Observatory (SDO). *Solar Physics* **275**(1-2), 207–227 (2012) <https://doi.org/10.1007/s11207-011-9834-2>
- [69] Borrero, J.M., Tomczyk, S., Kubo, M., Socas-Navarro, H., Schou, J., Couvidat, S., Bogart, R.: VFISV: Very Fast Inversion of the Stokes Vector for the Helioseismic and Magnetic Imager. *Solar Physics* **273**(1), 267–293 (2011) <https://doi.org/10.1007/s11207-010-9515-6> [arXiv:0901.2702](https://arxiv.org/abs/0901.2702) [astro-ph.IM]
- [70] Bommier, V.: Milne-Eddington inversion for unresolved magnetic structures in the quiet Sun photosphere. *Journal of Geophysical Research (Space Physics)* **121**(6), 5025–5040 (2016) <https://doi.org/10.1002/2016JA022368>
- [71] Metcalf, T.R.: Resolving the 180-degree ambiguity in vector magnetic field measurements: The ‘minimum’ energy solution. *Solar Physics* **155**(2), 235–242 (1994) <https://doi.org/10.1007/BF00680593>
- [72] Leka, K.D., Barnes, G., Crouch, A.D., Metcalf, T.R., Gary, G.A., Jing, J., Liu, Y.: Resolving the 180° Ambiguity in Solar Vector Magnetic Field Data: Evaluating the Effects of Noise, Spatial Resolution, and Method Assumptions. *Solar Physics* **260**(1), 83–108 (2009) <https://doi.org/10.1007/s11207-009-9440-8>
- [73] Leka, K.D., Wagner, E.L., Griñón-Marín, A.B., Bommier, V., Higgins, R.E.L.: On Identifying and Mitigating Bias in Inferred Measurements for Solar Vector Magnetic-Field Data. *Solar Physics* **297**(9), 121 (2022) <https://doi.org/10.1007/s11207-022-02039-9> [arXiv:2207.11572](https://arxiv.org/abs/2207.11572) [astro-ph.SR]
- [74] Wiegmann, T., Inhester, B., Sakurai, T.: Preprocessing of Vector Magnetograph Data for a Nonlinear Force-Free Magnetic Field Reconstruction. *Solar Physics* **233**(2), 215–232 (2006) <https://doi.org/10.1007/s11207-006-2092-z> [arXiv:astro-ph/0612641](https://arxiv.org/abs/astro-ph/0612641) [astro-ph]



- [75] Valori, G., Kliem, B., Török, T., Titov, V.S.: Testing magnetofrictional extrapolation with the Titov-Démoulin model of solar active regions. *A&A* **519**, 44 (2010) <https://doi.org/10.1051/0004-6361/201014416> arXiv:1005.0254 [astro-ph.SR]
- [76] Thalmann, J.K., Linan, L., Pariat, E., Valori, G.: On the Reliability of Magnetic Energy and Helicity Computations Based on Nonlinear Force-free Coronal Magnetic Field Models. *ApJ letters* **880**(1), 6 (2019) <https://doi.org/10.3847/2041-8213/ab2e73> arXiv:1907.01179 [astro-ph.SR]
- [77] Guo, Y., Pariat, E., Valori, G., Anfinogentov, S., Chen, F., Georgoulis, M.K., Liu, Y., Moraitis, K., Thalmann, J.K., Yang, S.: Magnetic Helicity Estimations in Models and Observations of the Solar Magnetic Field. III. Twist Number Method. *ApJ* **840**(1), 40 (2017) <https://doi.org/10.3847/1538-4357/aa6aa8> arXiv:1704.02096 [astro-ph.SR]
- [78] Chiu, Y.T., Hilton, H.H.: Exact Green's function method of solar force-free magnetic-field computations with constant alpha . I. Theory and basic test cases. *ApJ* **212**, 873–885 (1977) <https://doi.org/10.1086/155111>
- [79] Aulanier, G., Démoulin, P., Schmieder, B., Fang, C., Tang, Y.H.: Magnetohydrostatic Model of a Bald-Patch Flare. *Solar Physics* **183**(2), 369–388 (1998) <https://doi.org/10.1023/A:1005003426798>
- [80] Mandrini, C.H., Schmieder, B., Démoulin, P., Guo, Y., Cristiani, G.D.: Topological Analysis of Emerging Bipole Clusters Producing Violent Solar Events. *Solar Physics* **289**(6), 2041–2071 (2014) <https://doi.org/10.1007/s11207-013-0458-6> arXiv:1312.3359 [astro-ph.SR]
- [81] Guo, Y., Démoulin, P., Schmieder, B., Ding, M.D., Vargas Domínguez, S., Liu, Y.: Recurrent coronal jets induced by repetitively accumulated electric currents. *A&A* **555**, 19 (2013) <https://doi.org/10.1051/0004-6361/201321229> arXiv:1305.0902 [astro-ph.SR]
- [82] Wiegmann, T., Sakurai, T.: Solar force-free magnetic fields. *Living Reviews in Solar Physics* **18**(1), 1 (2021) <https://doi.org/10.1007/s41116-020-00027-4> arXiv:1208.4693 [astro-ph.SR]
- [83] Schmieder, B., Aulanier, G., Demoulin, P., van Driel-Gesztelyi, L., Roudier, T., Nitta, N., Cauzzi, G.: Magnetic reconnection driven by emergence of sheared magnetic field. *A&A* **325**, 1213–1225 (1997)
- [84] Mandrini, C.H., Démoulin, P., Van Driel-Gesztelyi, L., Schmieder, B., Cauzzi, G., Hofmann, A.: 3D Magnetic Reconnection at an X-Ray Bright Point. *Solar Physics* **168**(1), 115–133 (1996) <https://doi.org/10.1007/BF00145829>
- [85] Dalmasse, K., Chandra, R., Schmieder, B., Aulanier, G.: Can we explain atypical

- solar flares? *A&A* **574**, 37 (2015) <https://doi.org/10.1051/0004-6361/201323206> [arXiv:1410.8194](https://arxiv.org/abs/1410.8194) [astro-ph.SR]
- [86] Green, L.M., Valori, G., Zuccarello, F.P., Zharkov, S., Matthews, S.A., Guglielmino, S.L.: The 2013 February 17 Sunquake in the Context of the Active Region's Magnetic Field Configuration. *ApJ* **849**(1), 40 (2017) <https://doi.org/10.3847/1538-4357/aa8db6> [arXiv:1709.04874](https://arxiv.org/abs/1709.04874) [astro-ph.SR]
- [87] Zuccarello, F.P., Aulanier, G., Gilchrist, S.A.: Critical Decay Index at the Onset of Solar Eruptions. *ApJ* **814**(2), 126 (2015) <https://doi.org/10.1088/0004-637X/814/2/126> [arXiv:1510.03713](https://arxiv.org/abs/1510.03713) [astro-ph.SR]
- [88] Joshi, N.C., Zhu, X., Schmieder, B., Aulanier, G., Janvier, M., Joshi, B., Magara, T., Chandra, R., Inoue, S.: Generalization of the Magnetic Field Configuration of Typical and Atypical Confined Flares. *ApJ* **871**(2), 165 (2019) <https://doi.org/10.3847/1538-4357/aaf3b5> [arXiv:1811.01228](https://arxiv.org/abs/1811.01228) [astro-ph.SR]
- [89] Hood, A.W., Priest, E.R.: Critical conditions for magnetic instabilities in force-free coronal loops. *Geophysical and Astrophysical Fluid Dynamics* **17**(1), 297–318 (1981) <https://doi.org/10.1080/03091928108243687>
- [90] Moore, R.L., Labonte, B.J.: The filament eruption in the 3B flare of July 29, 1973 - Onset and magnetic field configuration. In: Dryer, M., Tandberg-Hanssen, E. (eds.) *Solar and Interplanetary Dynamics*, vol. 91, pp. 207–210 (1980)
- [91] Jiang, C., Bian, X., Feng, X., Zhou, Z., Duan, A., Wang, X., Zou, P., Zuo, P., Wang, Y.: Developments of a fundamental mechanism for initiation of solar eruptions. *Reviews of Modern Plasma Physics* **8**(1), 18 (2024) <https://doi.org/10.1007/s41614-024-00155-6>
- [92] Yeates, A.R.: The Minimal Helicity of Solar Coronal Magnetic Fields. *ApJ letters* **898**(2), 49 (2020) <https://doi.org/10.3847/2041-8213/aba762> [arXiv:2007.10649](https://arxiv.org/abs/2007.10649) [astro-ph.SR]
- [93] Zhu, X.S., Wang, H.N., Du, Z.L., Fan, Y.L.: Forced Field Extrapolation: Testing a Magnetohydrodynamic (MHD) Relaxation Method with a Flux-rope Emergence Model. *ApJ* **768**(2), 119 (2013) <https://doi.org/10.1088/0004-637X/768/2/119>
- [94] Jiang, C., Feng, X.: Extrapolation of the Solar Coronal Magnetic Field from SDO/HMI Magnetogram by a CESE-MHD-NLFFF Code. *ApJ* **769**(2), 144 (2013) <https://doi.org/10.1088/0004-637X/769/2/144> [arXiv:1304.2979](https://arxiv.org/abs/1304.2979) [astro-ph.SR]
- [95] Guo, Y., Xia, C., Keppens, R.: Magneto-frictional Modeling of Coronal Non-linear Force-free Fields. II. Application to Observations. *ApJ* **828**(2), 83 (2016) <https://doi.org/10.3847/0004-637X/828/2/83>

- [96] Guo, Y., Xia, C., Keppens, R., Valori, G.: Magneto-frictional Modeling of Coronal Nonlinear Force-free Fields. I. Testing with Analytic Solutions. *ApJ* **828**(2), 82 (2016) <https://doi.org/10.3847/0004-637X/828/2/82>
- [97] Jiang, C., Feng, X., Zhang, J., Zhong, D.: AMR Simulations of Magnetohydrodynamic Problems by the CESE Method in Curvilinear Coordinates. *Solar Physics* **267**(2), 463–491 (2010) <https://doi.org/10.1007/s11207-010-9649-6>
- [98] Cheung, M.C.M., De Pontieu, B., Tarbell, T.D., Fu, Y., Tian, H., Testa, P., Reeves, K.K., Martínez-Sykora, J., Boerner, P., Wülser, J.P., Lemen, J., Title, A.M., Hurlburt, N., Kleint, L., Kankelborg, C., Jaeggli, S., Golub, L., McKillop, S., Saar, S., Carlsson, M., Hansteen, V.: Homologous Helical Jets: Observations By IRIS, SDO, and Hinode and Magnetic Modeling With Data-Driven Simulations. *ApJ* **801**(2), 83 (2015) <https://doi.org/10.1088/0004-637X/801/2/83> [arXiv:1501.01593](https://arxiv.org/abs/1501.01593) [astro-ph.SR]
- [99] Kilpua, E.K.J., Pomoell, J., Price, D., Sarkar, R., Asvestari, E.: Estimating the magnetic structure of an erupting CME flux rope from AR12158 using data-driven modelling. *Frontiers in Astronomy and Space Sciences* **8**, 35 (2021) <https://doi.org/10.3389/fspas.2021.631582>
- [100] Lumme, E., Pomoell, J., Price, D.J., Kilpua, E.K.J., Kazachenko, M.D., Fisher, G.H., Welsch, B.T.: Data-driven, time-dependent modeling of pre-eruptive coronal magnetic field configuration at the periphery of NOAA AR 11726. *A&A* **658**, 200 (2022) <https://doi.org/10.1051/0004-6361/202038744>
- [101] Guo, J.H., Ni, Y.W., Guo, Y., Xia, C., Schmieder, B., Poedts, S., Zhong, Z., Zhou, Y.H., Yu, F., Chen, P.F.: Data-driven Modeling of a Coronal Magnetic Flux Rope: From Birth to Death. *ApJ* **961**(1), 140 (2024) <https://doi.org/10.3847/1538-4357/ad088d> [arXiv:2310.19617](https://arxiv.org/abs/2310.19617) [astro-ph.SR]
- [102] Wheatland, M.S., Sturrock, P.A., Roumeliotis, G.: An Optimization Approach to Reconstructing Force-free Fields. *ApJ* **540**(2), 1150–1155 (2000) <https://doi.org/10.1086/309355>
- [103] Wiegmann, T.: Optimization code with weighting function for the reconstruction of coronal magnetic fields. *Solar Physics* **219**(1), 87–108 (2004) <https://doi.org/10.1023/B:SOLA.0000021799.39465.36> [arXiv:0802.0124](https://arxiv.org/abs/0802.0124) [astro-ph]
- [104] Sakurai, T.: Calculation of force-free magnetic field with non-constant  $\alpha$ . *Solar Physics* **69**(2), 343–359 (1981) <https://doi.org/10.1007/BF00149999>
- [105] Amari, T., Boulmezaoud, T.Z., Aly, J.J.: Well posed reconstruction of the solar coronal magnetic field. *ApJ* **446**(2), 691–705 (2006) <https://doi.org/10.1051/0004-6361:20054076>
- [106] Chiu, Y.T., Hilton, H.H.: Exact Green’s function method of solar force-free

- magnetic-field computations with constant alpha . I. Theory and basic test cases. *ApJ* **212**, 873–885 (1977) <https://doi.org/10.1086/155111>
- [107] Xia, C., Teunissen, J., El Mellah, I., Chané, E., Keppens, R.: MPI-AMRVAC 2.0 for Solar and Astrophysical Applications. *ApJS* **234**(2), 30 (2018) <https://doi.org/10.3847/1538-4365/aaa6c8> arXiv:1710.06140 [astro-ph.SR]
- [108] Keppens, R., Popescu Braileanu, B., Zhou, Y., Ruan, W., Xia, C., Guo, Y., Claes, N., Bacchini, F.: MPI-AMRVAC 3.0: Updates to an open-source simulation framework. *A&A* **673**, 66 (2023) <https://doi.org/10.1051/0004-6361/202245359> arXiv:2303.03026 [astro-ph.IM]
- [109] Zhong, Z., Guo, Y., Ding, M.D., Fang, C., Hao, Q.: Transition from Circular-ribbon to Parallel-ribbon Flares Associated with a Bifurcated Magnetic Flux Rope. *ApJ* **871**(1), 105 (2019) <https://doi.org/10.3847/1538-4357/aaf863> arXiv:1812.10223 [astro-ph.SR]
- [110] Li, C., Fang, C., Li, Z., Ding, M.-D., Chen, P.-F., Chen, Z., Lin, L.-K., Chen, C.-Z., Chen, C.-Y., Tao, H.-J., You, W., Hao, Q., Dai, Y., Cheng, X., Guo, Y., Hong, J., An, M.-J., Cheng, W.-Q., Chen, J.-X., Wang, W., Zhang, W.: Chinese H $\alpha$  Solar Explorer (CHASE) - a complementary space mission to the ASO-S. *Research in Astronomy and Astrophysics* **19**(11), 165 (2019) <https://doi.org/10.1088/1674-4527/19/11/165>
- [111] Li, C., Fang, C., Li, Z., Ding, M., Chen, P., Qiu, Y., You, W., Yuan, Y., An, M., Tao, H., Li, X., Chen, Z., Liu, Q., Mei, G., Yang, L., Zhang, W., Cheng, W., Chen, J., Chen, C., Gu, Q., Huang, Q., Liu, M., Han, C., Xin, H., Chen, C., Ni, Y., Wang, W., Rao, S., Li, H., Lu, X., Wang, W., Lin, J., Jiang, Y., Meng, L., Zhao, J.: The Chinese H $\alpha$  Solar Explorer (CHASE) mission: An overview. *Science China Physics, Mechanics, and Astronomy* **65**(8), 289602 (2022) <https://doi.org/10.1007/s11433-022-1893-3> arXiv:2205.05962 [astro-ph.SR]
- [112] Prasad, A., Kumar, S., Sterling, A.C., Moore, R.L., Aulanier, G., Bhattacharyya, R., Hu, Q.: Formation of an observed eruptive flux rope above the torus instability threshold through tether-cutting magnetic reconnection. *A&A* **677**, 43 (2023) <https://doi.org/10.1051/0004-6361/202346267> arXiv:2307.06572 [astro-ph.SR]
- [113] Wang, X., Jiang, C., Feng, X.: MHD Simulation of a Solar Eruption from Active Region 11429 Driven by a Photospheric Velocity Field. *apJ letters* **942**(2), 41 (2023) <https://doi.org/10.3847/2041-8213/acaec3> arXiv:2301.00144 [astro-ph.SR]
- [114] Low, B.C., Lou, Y.Q.: Modeling Solar Force-free Magnetic Fields. *ApJ* **352**, 343 (1990) <https://doi.org/10.1086/168541>
- [115] van Ballegoijen, A.A.: Observations and Modeling of a Filament on the Sun. *ApJ* **612**(1), 519–529 (2004) <https://doi.org/10.1086/422512>

- [116] Bobra, M.G., van Ballegoijen, A.A., DeLuca, E.E.: Modeling Nonpotential Magnetic Fields in Solar Active Regions. *ApJ* **672**(2), 1209–1220 (2008) <https://doi.org/10.1086/523927>
- [117] Su, Y., van Ballegoijen, A., Schmieder, B., Berlicki, A., Guo, Y., Golub, L., Huang, G.: Flare Energy Build-up in a Decaying Active Region Near a Coronal Hole. *ApJ* **704**(1), 341–353 (2009) <https://doi.org/10.1088/0004-637X/704/1/341>
- [118] Su, Y., van Ballegoijen, A., McCauley, P., Ji, H., Reeves, K.K., DeLuca, E.E.: Magnetic Structure and Dynamics of the Erupting Solar Polar Crown Prominence on 2012 March 12. *ApJ* **807**(2), 144 (2015) <https://doi.org/10.1088/0004-637X/807/2/144> [arXiv:1505.06826](https://arxiv.org/abs/1505.06826) [astro-ph.SR]
- [119] Mackay, D.H., Schmieder, B., López Ariste, A., Su, Y.: Modelling and observations: Comparison of the magnetic field properties in a prominence. *A&A* **637**, 3 (2020) <https://doi.org/10.1051/0004-6361/201936656>
- [120] Lemen, J.R., Title, A.M., Akin, D.J., Boerner, P.F., Chou, C., Drake, J.F., Duncan, D.W., Edwards, C.G., Friedlaender, F.M., Heyman, G.F., Hurlburt, N.E., Katz, N.L., Kushner, G.D., Levay, M., Lindgren, R.W., Mathur, D.P., McFeaters, E.L., Mitchell, S., Rehse, R.A., Schrijver, C.J., Springer, L.A., Stern, R.A., Tarbell, T.D., Wuelser, J.-P., Wolfson, C.J., Yanari, C., Bookbinder, J.A., Cheimets, P.N., Caldwell, D., Deluca, E.E., Gates, R., Golub, L., Park, S., Podgorski, W.A., Bush, R.I., Scherrer, P.H., Gummin, M.A., Smith, P., Auker, G., Jerram, P., Pool, P., Soufli, R., Windt, D.L., Beardsley, S., Clapp, M., Lang, J., Waltham, N.: The Atmospheric Imaging Assembly (AIA) on the Solar Dynamics Observatory (SDO). *Solar Physics* **275**(1-2), 17–40 (2012) <https://doi.org/10.1007/s11207-011-9776-8>
- [121] Titov, V.S., Downs, C., Mikić, Z., Török, T., Linker, J.A., Caplan, R.M.: Regularized Biot-Savart Laws for Modeling Magnetic Flux Ropes. *ApJ letters* **852**(2), 21 (2018) <https://doi.org/10.3847/2041-8213/aaa3da> [arXiv:1712.06708](https://arxiv.org/abs/1712.06708) [astro-ph.SR]
- [122] Guo, J.H., Ni, Y.W., Zhou, Y.H., Guo, Y., Schmieder, B., Chen, P.F.: Prominence fine structures in weakly twisted and highly twisted magnetic flux ropes. *A&A* **667**, 89 (2022) <https://doi.org/10.1051/0004-6361/202244253> [arXiv:2209.06712](https://arxiv.org/abs/2209.06712) [astro-ph.SR]
- [123] Guo, Y., Zhong, Z., Ding, M.D., Chen, P.F., Xia, C., Keppens, R.: Data-constrained Magnetohydrodynamic Simulation of a Long-duration Eruptive Flare. *ApJ* **919**(1), 39 (2021) <https://doi.org/10.3847/1538-4357/ac10c8> [arXiv:2106.15080](https://arxiv.org/abs/2106.15080) [astro-ph.SR]
- [124] Guo, J.H., Ni, Y.W., Qiu, Y., Zhong, Z., Guo, Y., Chen, P.F.: Magnetic Twists of Solar Filaments. *ApJ* **917**(2), 81 (2021) <https://doi.org/10.3847/1538-4357/>

ac0cef arXiv:2107.02580 [astro-ph.SR]

- [125] Fan, Y.: An Improved Magnetohydrodynamic Simulation of the 2006 December 13 Coronal Mass Ejection of NOAA Active Region 10930. *ApJ* **941**(1), 61 (2022) <https://doi.org/10.3847/1538-4357/aca0ec> arXiv:2211.03736 [astro-ph.SR]
- [126] Devi, P., Chandra, R., Awasthi, A.K., Schmieder, B., Joshi, R.: Extreme-Ultraviolet Wave and Accompanying Loop Oscillations. *Solar Physics* **297**(12), 153 (2022) <https://doi.org/10.1007/s11207-022-02082-6> arXiv:2211.07438 [astro-ph.SR]
- [127] Chen, P.F., Wu, S.T., Shibata, K., Fang, C.: Evidence of EIT and Moreton Waves in Numerical Simulations. *ApJ letters* **572**(1), 99–102 (2002) <https://doi.org/10.1086/341486>
- [128] Chen, P.F.: The Relation Between EIT Waves and Coronal Mass Ejections. *ApJ letters* **698**(2), 112–115 (2009) <https://doi.org/10.1088/0004-637X/698/2/L112> arXiv:0905.3272 [astro-ph.SR]
- [129] Liu, L., Cheng, X., Wang, Y., Zhou, Z.: Formation of a Magnetic Flux Rope in the Early Emergence Phase of NOAA Active Region 12673. *ApJ* **884**(1), 45 (2019) <https://doi.org/10.3847/1538-4357/ab3c6c> arXiv:1908.06360 [astro-ph.SR]
- [130] Price, D.J., Pomoell, J., Lumme, E., Kilpua, E.K.J.: Time-dependent data-driven coronal simulations of AR 12673 from emergence to eruption. *A&A* **628**, 114 (2019) <https://doi.org/10.1051/0004-6361/201935535>
- [131] Inoue, S., Bamba, Y.: An MHD Modeling of the Successive X2.2 and X9.3 Solar Flares of 2017 September 6. *ApJ* **914**(1), 71 (2021) <https://doi.org/10.3847/1538-4357/abf835> arXiv:2104.06639 [astro-ph.SR]
- [132] Liu, L., Cheng, X., Wang, Y., Zhou, Z., Guo, Y., Cui, J.: Rapid Buildup of a Magnetic Flux Rope during a Confined X2.2 Class Flare in NOAA AR 12673. *ApJ Letters* **867**(1), 5 (2018) <https://doi.org/10.3847/2041-8213/aae826> arXiv:1810.04424 [astro-ph.SR]
- [133] Chintzoglou, G., Zhang, J., Cheung, M.C.M., Kazachenko, M.: The Origin of Major Solar Activity: Collisional Shearing between Nonconjugated Polarities of Multiple Bipoles Emerging within Active Regions. *ApJ* **871**(1), 67 (2019) <https://doi.org/10.3847/1538-4357/aaef30> arXiv:1811.02186 [astro-ph.SR]
- [134] Zhong, Z., Guo, Y., Wiegmann, T., Ding, M.D., Chen, Y.: Unveiling the Mechanism for the Rapid Acceleration Phase in a Solar Eruption. *ApJ Letters* **947**(1), 2 (2023) <https://doi.org/10.3847/2041-8213/acc6ce> arXiv:2303.14050 [astro-ph.SR]

- [135] Jiang, C., Feng, X., Bian, X., Zou, P., Duan, A., Yan, X., Hu, Q., He, W., Wang, X., Zuo, P., Wang, Y.: Data-driven MHD simulation of a sunspot rotating active region leading to solar eruption. arXiv e-prints, 2308–06977 (2023) <https://doi.org/10.48550/arXiv.2308.06977> arXiv:2308.06977 [astro-ph.SR]
- [136] Daei, Pomoell, J., Price, D. J., Kumari, A., Good, S., Kilpua, E. K. J.: Modeling the formation and eruption of coronal structures by linking data-driven magnetofrictional and mhd simulations for ar 12673. *A&A* **676**, 141 (2023) <https://doi.org/10.1051/0004-6361/202346183>
- [137] Schuck, P.W.: Tracking Vector Magnetograms with the Magnetic Induction Equation. *ApJ* **683**(2), 1134–1152 (2008) <https://doi.org/10.1086/589434> arXiv:0803.3472 [astro-ph]
- [138] Welsch, B.T., Abbett, W.P., De Rosa, M.L., Fisher, G.H., Georgoulis, M.K., Kusano, K., Longcope, D.W., Ravindra, B., Schuck, P.W.: Tests and Comparisons of Velocity-Inversion Techniques. *ApJ* **670**(2), 1434–1452 (2007) <https://doi.org/10.1086/522422>
- [139] Wang, X., Jiang, C., Feng, X., Wang, B., Chen, B.: A comparative study of data-driven MHD simulations of solar coronal evolution with photospheric flows derived from two different approaches. *Frontiers in Astronomy and Space Sciences* **10**, 1157304 (2023) <https://doi.org/10.3389/fspas.2023.1157304>
- [140] Toriumi, S., Takasao, S., Cheung, M.C.M., Jiang, C., Guo, Y., Hayashi, K., Inoue, S.: Comparative Study of Data-driven Solar Coronal Field Models Using a Flux Emergence Simulation as a Ground-truth Data Set. *ApJ* **890**(2), 103 (2020) <https://doi.org/10.3847/1538-4357/ab6b1f> arXiv:2001.03721 [astro-ph.SR]
- [141] Mitra, P.K., Joshi, B., Prasad, A., Veronig, A.M., Bhattacharyya, R.: Successive Flux Rope Eruptions from  $\delta$ -sunspots Region of NOAA 12673 and Associated X-class Eruptive Flares on 2017 September 6. *ApJ* **869**(1), 69 (2018) <https://doi.org/10.3847/1538-4357/aaed26> arXiv:1810.13146 [astro-ph.SR]
- [142] Bamba, Y., Inoue, S., Hayashi, K.: The Role of a Tiny Brightening in a Huge Geoeffective Solar Eruption Leading to the St. Patrick’s Day Storm. *ApJ* **874**(1), 73 (2019) <https://doi.org/10.3847/1538-4357/ab06ff> arXiv:1902.04871 [astro-ph.SR]
- [143] Kusano, K., Bamba, Y., Yamamoto, T.T., Iida, Y., Toriumi, S., Asai, A.: Magnetic Field Structures Triggering Solar Flares and Coronal Mass Ejections. *ApJ* **760**(1), 31 (2012) <https://doi.org/10.1088/0004-637X/760/1/31> arXiv:1210.0598 [astro-ph.SR]
- [144] Amari, T., Canou, A., Aly, J.-J., Delyon, F., Alauzet, F.: Magnetic cage and rope as the key for solar eruptions. *Nature* **554**(7691), 211–215 (2018) <https://doi.org/10.1038/nature24671>

- [145] Zuccarello, F.P., Chandra, R., Schmieder, B., Aulanier, G., Joshi, R.: Transition from eruptive to confined flares in the same active region. *A&A* **601**, 26 (2017) <https://doi.org/10.1051/0004-6361/201629836> arXiv:1702.02477 [astro-ph.SR]
- [146] Zhou, Z., Cheng, X., Zhang, J., Wang, Y., Wang, D., Liu, L., Zhuang, B., Cui, J.: Why Do Torus-unstable Solar Filaments Experience Failed Eruptions? *ApJ Letters* **877**(2), 28 (2019) <https://doi.org/10.3847/2041-8213/ab21cb> arXiv:1905.00224 [astro-ph.SR]
- [147] Jiang, C., Duan, A., Zou, P., Zhou, Z., Bian, X., Feng, X., Zuo, P., Wang, Y.: A model of failed solar eruption initiated and destructed by magnetic reconnection. *Monthly Notices of the Royal Academy Society* **525**(4), 5857–5867 (2023) <https://doi.org/10.1093/mnras/stad2658> arXiv:2307.15847 [astro-ph.SR]
- [148] Moore, R.L., Sterling, A.C., Hudson, H.S., Lemen, J.R.: Onset of the Magnetic Explosion in Solar Flares and Coronal Mass Ejections. *ApJ* **552**(2), 833–848 (2001) <https://doi.org/10.1086/320559>
- [149] Török, T., Kliem, B., Titov, V.S.: Ideal kink instability of a magnetic loop equilibrium. *A&A* **413**, 27–30 (2004) <https://doi.org/10.1051/0004-6361:20031691> arXiv:astro-ph/0311198 [astro-ph]
- [150] Démoulin, P., Aulanier, G.: Criteria for Flux Rope Eruption: Non-equilibrium Versus Torus Instability. *ApJ* **718**(2), 1388–1399 (2010) <https://doi.org/10.1088/0004-637X/718/2/1388> arXiv:1006.1785 [astro-ph.SR]
- [151] Zuccarello, F.P., Aulanier, G., Gilchrist, S.A.: The Apparent Critical Decay Index at the Onset of Solar Prominence Eruptions. *ApJ letter* **821**(2), 23 (2016) <https://doi.org/10.3847/2041-8205/821/2/L23>
- [152] Myers, C.E., Yamada, M., Ji, H., Yoo, J., Fox, W., Jara-Almonte, J., Savcheva, A., Deluca, E.E.: A dynamic magnetic tension force as the cause of failed solar eruptions. *Nature* **528**(7583), 526–529 (2015) <https://doi.org/10.1038/nature16188>
- [153] Myers, C.E., Yamada, M., Ji, H., Yoo, J., Jara-Almonte, J., Fox, W.: Laboratory study of low- $\beta$  forces in arched, line-tied magnetic flux ropes. *Physics of Plasmas* **23**(11), 112102 (2016) <https://doi.org/10.1063/1.4966691>
- [154] Chen, F., Cheung, M.C.M., Rempel, M., Chintzoglou, G.: Data-driven Radiative Magnetohydrodynamics Simulations with the MURaM Code. *ApJ* **949**(2), 118 (2023) <https://doi.org/10.3847/1538-4357/acc8c5> arXiv:2301.07621 [astro-ph.SR]
- [155] Wang, C., Chen, F., Ding, M., Lu, Z.: Radiative Magnetohydrodynamic Simulation of the Confined Eruption of a Magnetic Flux Rope: Unveiling the Driving and Constraining Forces. *ApJ* **956**(2), 106 (2023) <https://doi.org/10.3847/1538->



4357/acedfe arXiv:2308.11271 [astro-ph.SR]

- [156] Zhang, X.M., Guo, J.H., Guo, Y., Ding, M.D., Keppens, R.: Rotation and Confined Eruption of a Double Flux-rope System. *ApJ* **961**(2), 145 (2024) <https://doi.org/10.3847/1538-4357/ad1521> arXiv:2312.07406 [astro-ph.SR]
- [157] Joshi, R., Mandrini, C.H., Chandra, R., Schmieder, B., Cristiani, G.D., Mac Cormack, C., Démoulin, P., Cremades, H.: Analysis of the Evolution of a Multi-Ribbon Flare and Failed Filament Eruption. *Solar Physics* **297**(7), 81 (2022) <https://doi.org/10.1007/s11207-022-02021-5> arXiv:2206.00531 [astro-ph.SR]
- [158] Perri, B., Leitner, P., Brchnelova, M., Baratashvili, T., Kuźma, B., Zhang, F., Lani, A., Poedts, S.: COCONUT, a Novel Fast-converging MHD Model for Solar Corona Simulations: I. Benchmarking and Optimization of Polytropic Solutions. *ApJ* **936**(1), 19 (2022) <https://doi.org/10.3847/1538-4357/ac7237> arXiv:2205.03341 [astro-ph.SR]
- [159] Perri, B., Kuźma, B., Brchnelova, M., Baratashvili, T., Zhang, F., Leitner, P., Lani, A., Poedts, S.: COCONUT, a Novel Fast-converging MHD Model for Solar Corona Simulations. II. Assessing the Impact of the Input Magnetic Map on Space-weather Forecasting at Minimum of Activity. *ApJ* **943**(2), 124 (2023) <https://doi.org/10.3847/1538-4357/ac9799> arXiv:2210.06165 [astro-ph.SR]
- [160] Pomoell, J., Poedts, S.: EUHFORIA: European heliospheric forecasting information asset. *Journal of Space Weather and Space Climate* **8**, 35 (2018) <https://doi.org/10.1051/swsc/2018020>
- [161] Poedts, S.: Forecasting space weather with euhforia in the virtual space weather modeling centre. *Plasma Physics and Controlled Fusion* **61**(1), 014011 (2018) <https://doi.org/10.1088/1361-6587/aae048>

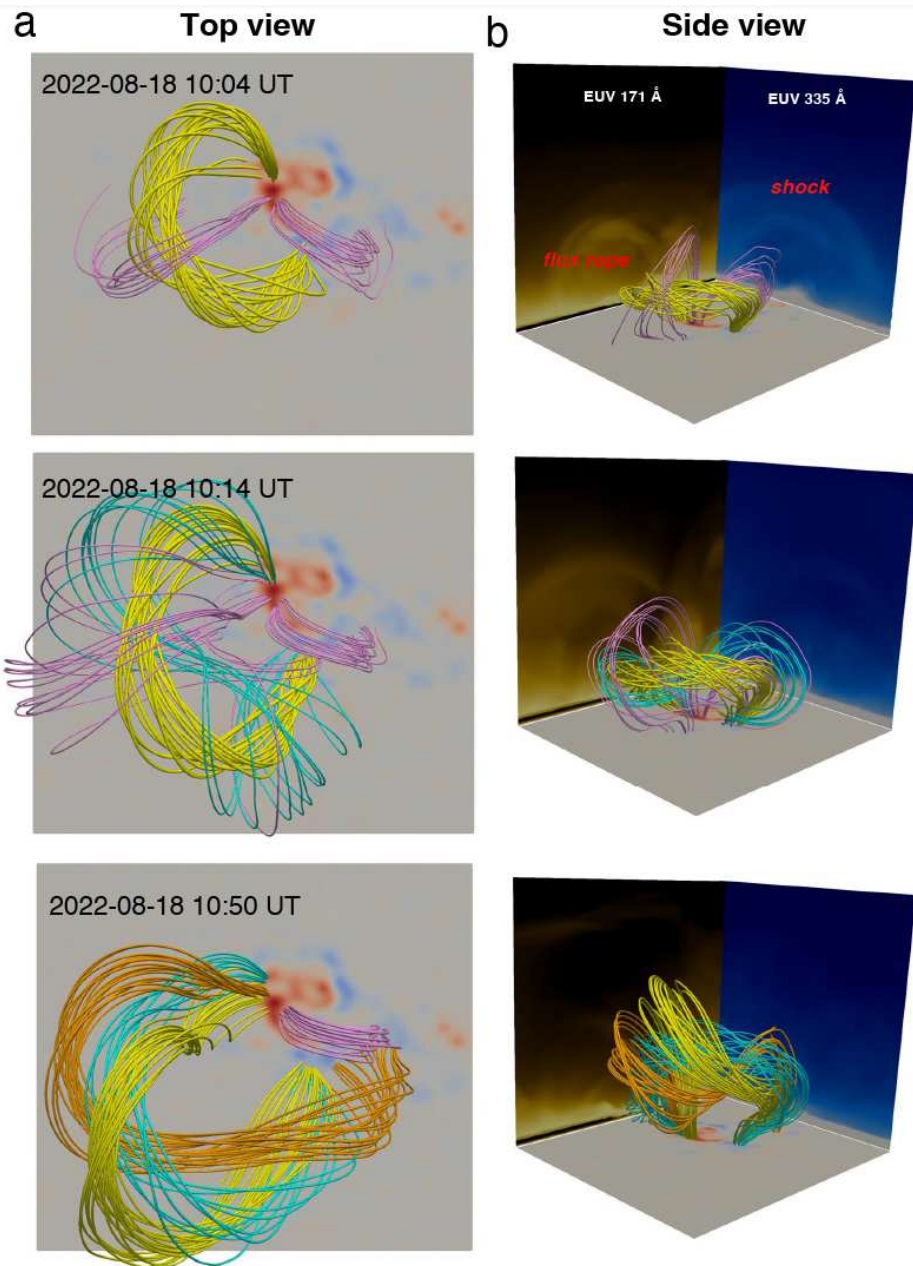


**Fig. 5** Top (left panels) and side (right panels) views of eruptive flux ropes obtained by a data-constrained MHD simulation. The synthesised EUV 171 Å and 335 Å images are shown in side views for comparison with SDO/AIA observations (adapted from Guo et al. [22]).

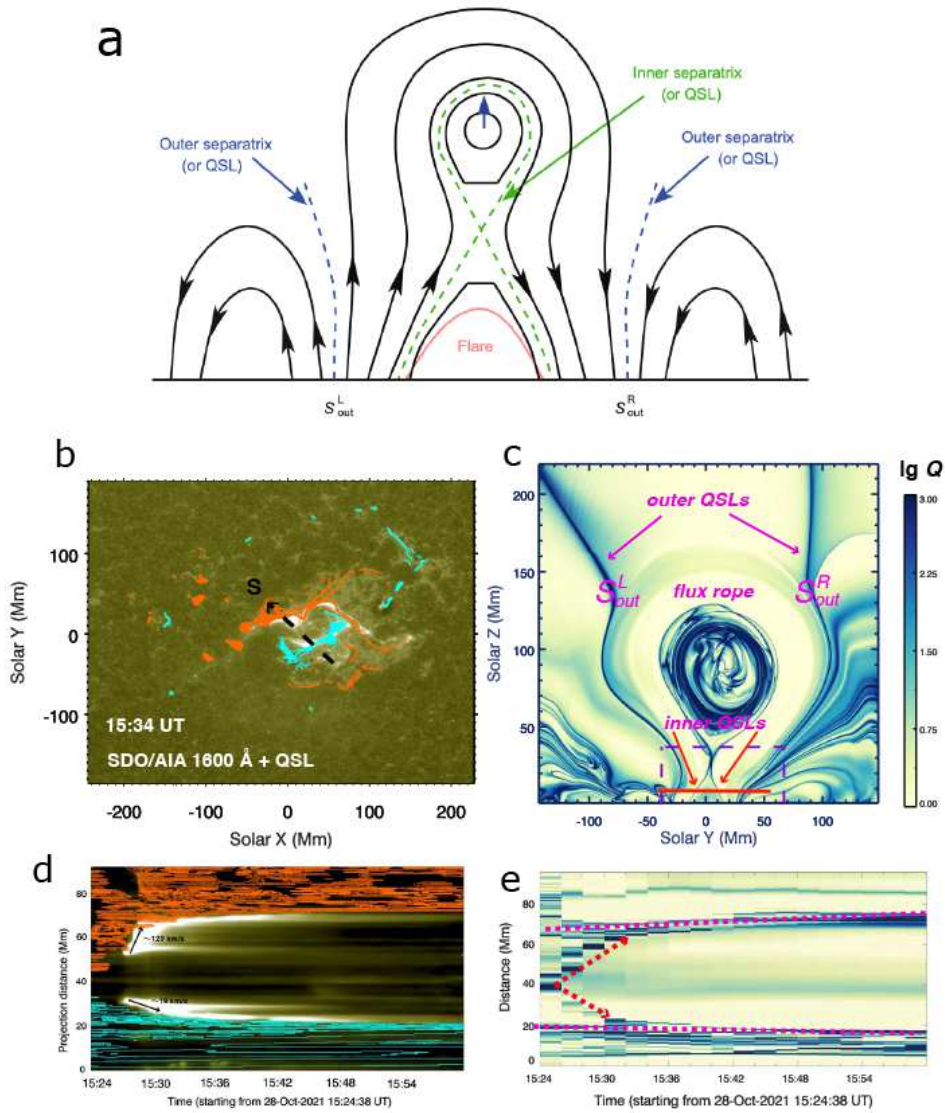


**Fig. 6** The stopping position of flare ribbons revealed by data-driven MHD simulation. Panel (a) shows the sketch of magnetic reconnection considering inner and outer QSLs, in which the separating inner QSLs correspond to flare ribbons in observations, and the outer QSLs determine the stopping position of flare ribbons. Panels (b)–(d) show the results of data-driven MHD simulation, validating the effects of inner and outer QSLs in explaining the dynamic evolution of flare ribbons. Panel (b) illustrates the  $Q$  distribution in the photosphere, overlaid on SDO/AIA 1600 Å observations. The black dashed line in panel (b) shows the slice for the time-distance diagram in panel (d). Panels (c) and (e) show the  $Q$  distribution on the side plane and dynamic evolution, respectively (adapted from Guo et al. [62]).

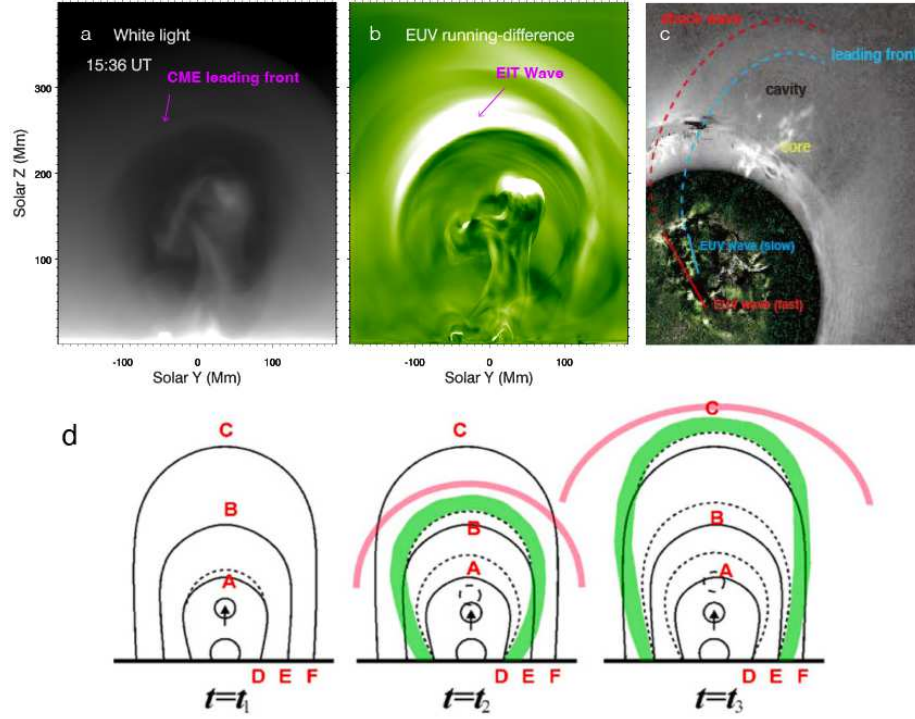


**Fig. 7** CME and EUV wave: (top panels) comparison between synthesised images (a, b) obtained with an MHD simulation and (c) observations by STEREO coronagraph (COR1) and EUV imagery (adapted from Guo et al. [62]). The fast- and slow-component of the EUV waves are roughly co-spatial with the shock and the CME frontal edge, respectively, while the EUV dimmings are co-spatial with the CME cavity. Panel (d) illustrated the sketch of the field-line stretching model in explaining the two components of EUV waves and the CME leading front (adapted from Chen [128]). The results of the data-driven model align with the field-line stretching model prediction.

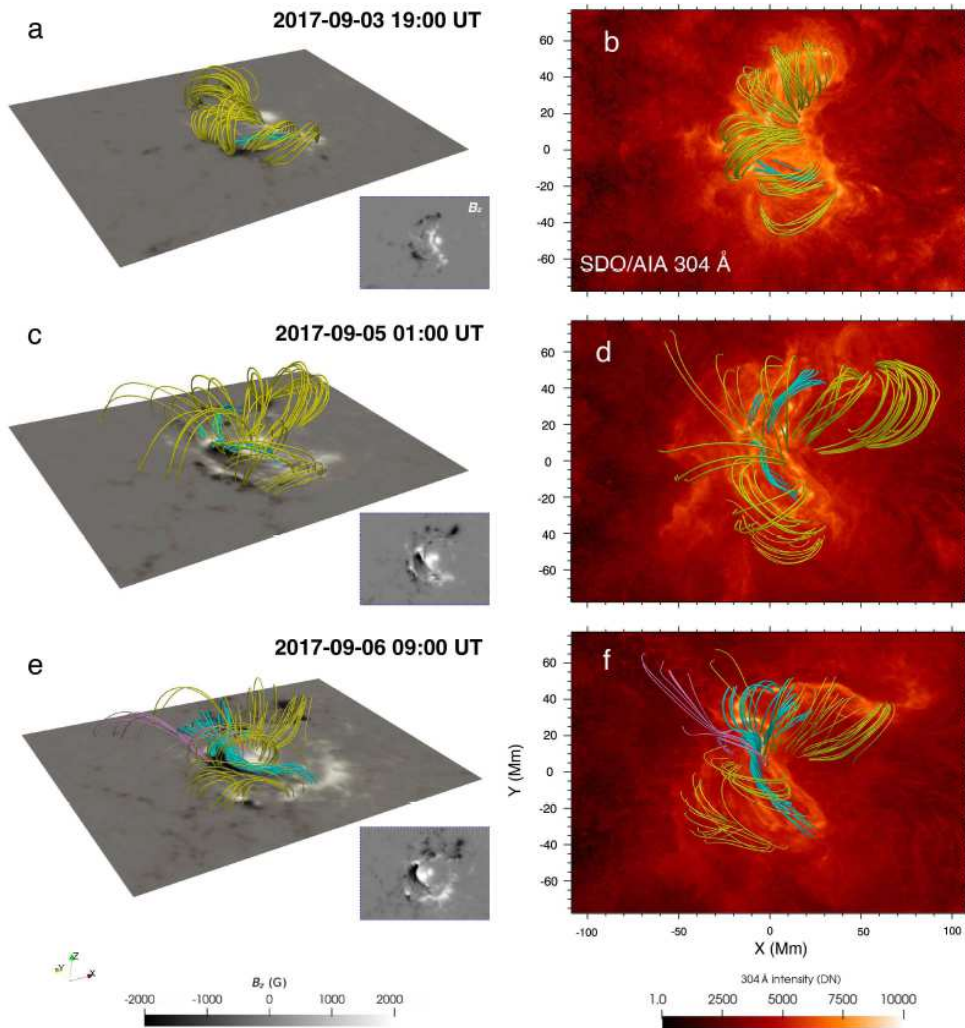


**Fig. 8** Left panels (a,c,e): Evolution of the flux rope with the magneto frictional method for three time steps and the corresponding magnetograms. Right panels (b,d,f) Comparison with AIA 304 Å images (adapted from Guo et al. [101]).

2017-09-05 01:00 UT

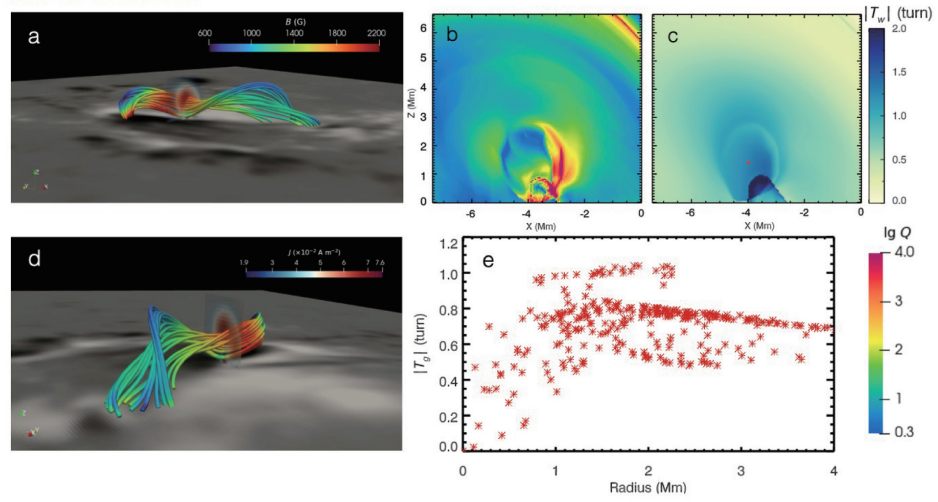


**Fig. 9** Twisted flux rope and magnetic topological structures obtained in a data-driven MHD simulation at 01:00 UT on 5 September 2017. Panels (a) and (d) illustrate two views of the formed flux rope, where the semi-transparent vertical slices across the flux rope represent the electric-current channel. Panels (b), (c) and (e) present the squashing factor ( $Q$ ), the twist ( $T_w$ ) maps in the same planes as panels (a) and (d). Panel (e) shows the  $T_g$  numbers of selected field lines along the distance from the red dot in panel (c) (adapted from Guo et al. [101]).

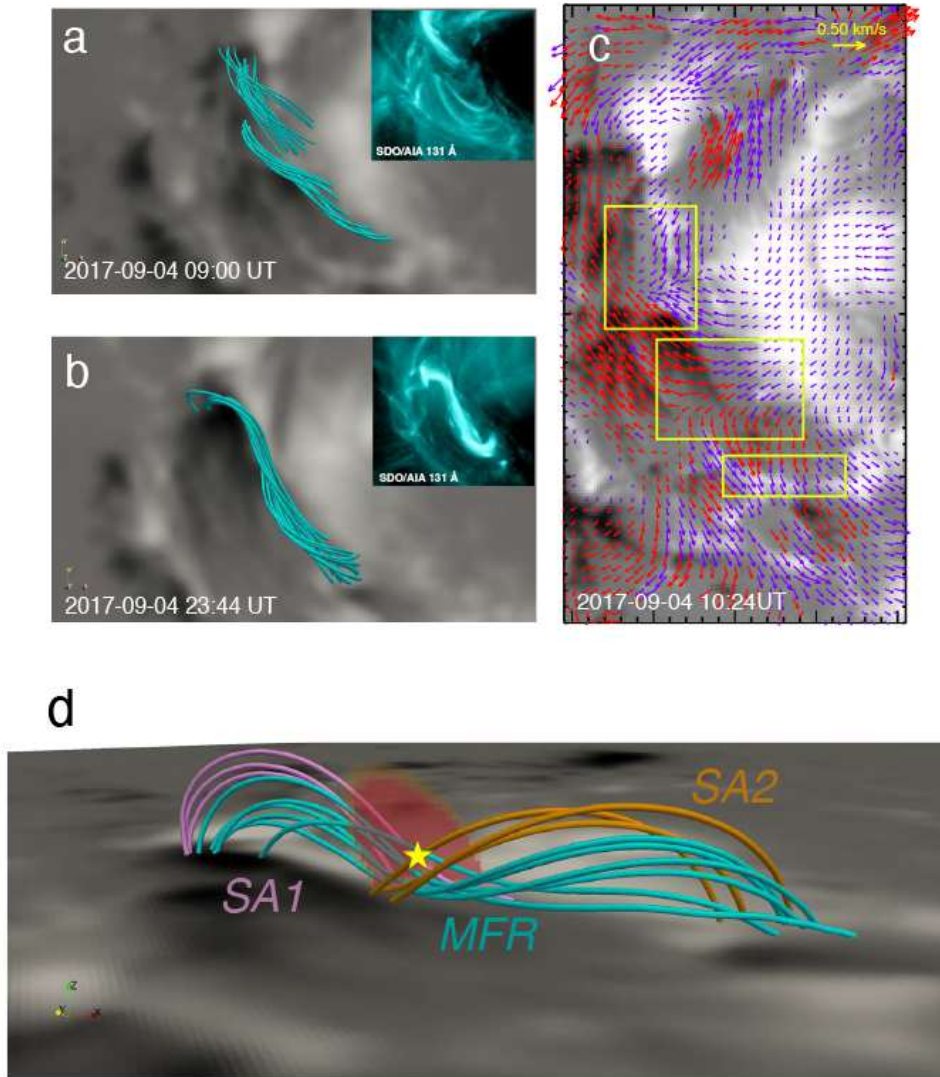


**Fig. 10** Formation of a flux rope simulated by the data-driven model. Panels (a) and (b) display the sheared arcades and flux ropes, respectively. The inserts show the SDO/AIA 131 Å images at the same time. Panel (c) displays the photospheric horizontal velocity fields. Panel (d) illustrates the reconnection configuration of the flux rope. The field lines traced from the current sheet depicted by the high  $J/B$  region can be divided into two groups of sheared arcades before reconnection (SA1 and SA2) and the newly reconnected flux rope (adapted from Guo et al. [101]).

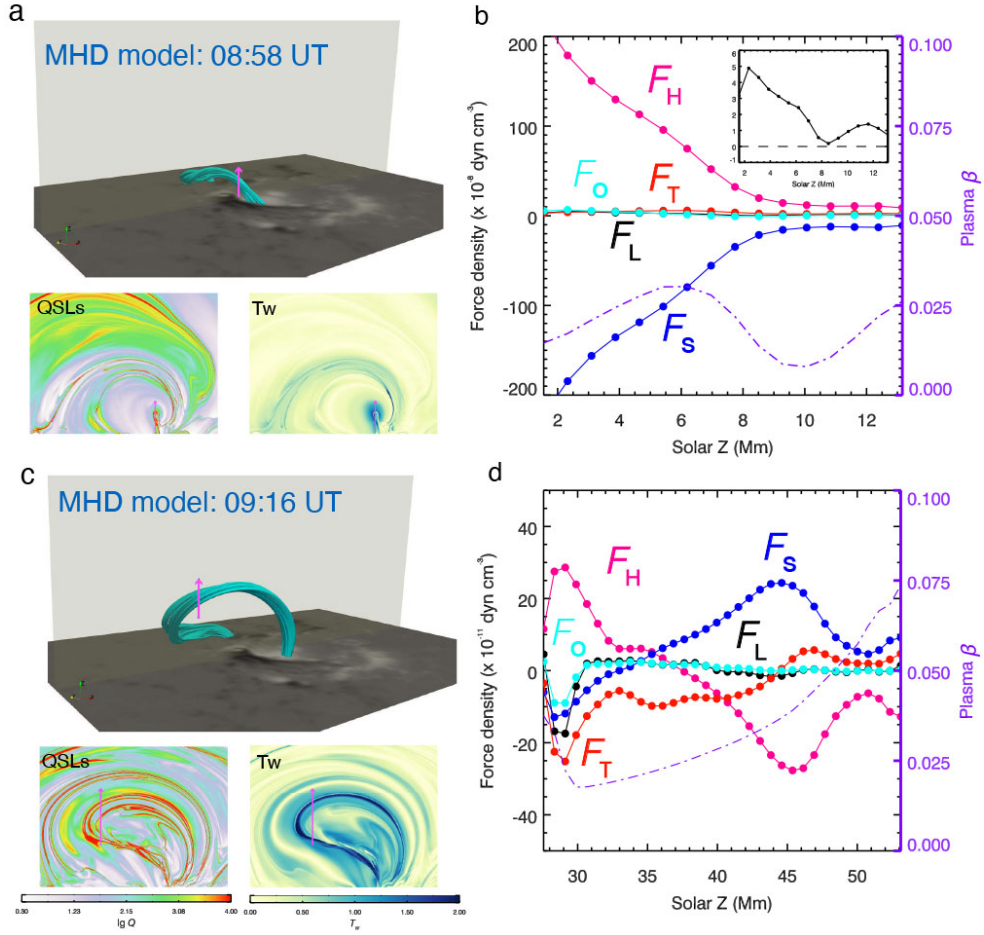


**Fig. 11** Lorentz force components acting upon the flux rope. Panels (a) and (c) show the 3D illustrations of the magnetic configuration and topology ( $Q$  and  $T_w$  distributions) at the initiation and the end of the eruption. Panels (b) and (d) show the distributions of the Lorentz force components, such as the net Lorentz force ( $F_L$ , black line), hoop force ( $F_H$ , pink line), strapping force ( $F_S$ , blue line), tension force ( $F_T$ , red line) and residual force ( $F_O$ , cyan line). The **purple dash-dotted line** represents the plasma  $\beta$  (adapted from Guo et al. [101]).



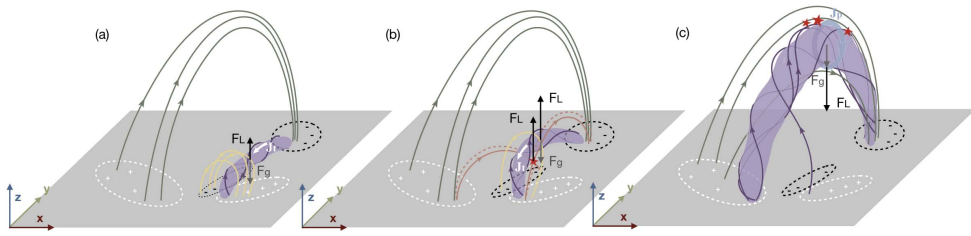


**Fig. 12** Sketch of the confined eruption describing the initiation and confinement of the solar eruption. The yellow and dark green lines represent the background toroidal and poloidal magnetic fields. The purple tubes show the flux ropes. The red pentagrams indicate the potential reconnection regions (adapted from Wang et al. [155]).

This figure "Chen\_model\_EUV.png" is available in "png" format from:

<http://arxiv.org/ps/2408.06595v1>

This figure "Diapositive1.jpeg" is available in "jpeg" format from:

<http://arxiv.org/ps/2408.06595v1>

This figure "Diapositive2.jpeg" is available in "jpeg" format from:

<http://arxiv.org/ps/2408.06595v1>

This figure "Diapositive3.jpeg" is available in "jpeg" format from:

<http://arxiv.org/ps/2408.06595v1>

This figure "Diapositive4.jpeg" is available in "jpeg" format from:

<http://arxiv.org/ps/2408.06595v1>

This figure "Diapositive5.jpeg" is available in "jpeg" format from:

<http://arxiv.org/ps/2408.06595v1>

This figure "Diapositive6.jpeg" is available in "jpeg" format from:

<http://arxiv.org/ps/2408.06595v1>



This figure "Diapositive7.jpeg" is available in "jpeg" format from:

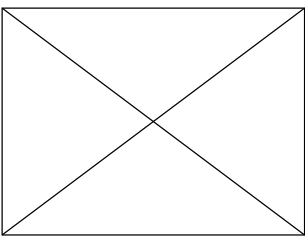
<http://arxiv.org/ps/2408.06595v1>

This figure "Diapositive8.jpeg" is available in "jpeg" format from:

<http://arxiv.org/ps/2408.06595v1>

This figure "Zhang\_can\_toroidal.png" is available in "png" format from:

<http://arxiv.org/ps/2408.06595v1>





This figure "present\_AAPPS\_Review\_slides.jpg" is available in "jpg" format from:

<http://arxiv.org/ps/2408.06595v1>